Revealing a hidden conducting state by manipulating the intracellular domains in $K_V10.1$ exposes the coupling between two gating mechanisms.

Reham Abdelaziz[1], Adam P. Tomczak[1], Andreas Neef[2]* and Luis A. Pardo[1]*

[1]Oncophysiology Group. Max Planck Institute for Multidisciplinary Sciences, City Campus.

[2]Neurophysics Laboratory. Göttingen Campus Institute for Dynamics of Biological Networks.

*For correspondence: pardo@mpinat.mpg.de; aneef@gwdg.de

Abstract

The *KCNH* family of potassium channels serves relevant physiological functions in both excitable and non-excitable cells, reflected in the massive consequences of mutations or pharmacological manipulation of their function. This group of channels shares structural homology with other voltage-gated K^+ channels, but the mechanisms of gating in this family show significant differences with respect to the canonical electromechanical coupling in these molecules. In particular, the large intracellular domains of *KCNH* channels play a crucial role in gating that is still only partly understood. Using *KCNH1*(K_V10.1) as a model, we have characterized the behavior of a series of modified channels that could not be explained by the current models. With electrophysiological and biochemical methods combined with mathematical modeling, we show that the uncovering of an open state can explain the behavior of the mutants. This open state, which is not detectable in wild-type channels, appears to lack the rapid flicker block of the conventional open state. Because it is accessed from deep closed states, it elucidates intermediate gating events well ahead of channel opening in the wild type. This allowed us to study gating steps prior to opening, which, for example, explain the mechanism of gating inhibition by Ca^{2+}-Calmodulin and generate a model that describes the characteristic features of *KCNH* channels gating.

Introduction

Voltage-gated potassium channels constitute a large family of proteins that allow K^+ flow upon changes in the membrane potential. Their general architecture consists of a tetrameric complex with six transmembrane segments (S1-S6) in each subunit to form a central pore with four voltage sensors at the periphery. S1 to S4 segments constitute the sensor domain, while S5 and S6 segments, together with the loop linking them, line the pore. The mechanism of voltage-dependent gating is well understood for several subfamilies, namely those closely related to the *Drosophila Shaker* channel (*KCNA* and *KCNB*). In this subset of families, the linker between the sensor and pore domains (S4-S5 linker) acts as a mechanical lever transferring the movement of the voltage sensor to the gate at the bottom of S6 in a neighboring subunit through physical interaction (Barros et al. 2020). Such trans-subunit interaction is commonly denoted "domain swapping." In other families, like the EAG family (*KCNH*) (Malak et al. 2019; Tomczak et al. 2017; Whicher and MacKinnon 2019), gating mechanics must be different because there is no domain swapping in the transmembrane regions, the S4-S5 segment is very short and does not form a helix (Whicher and MacKinnon 2016; Wang and MacKinnon 2017), and voltage-dependent gating occurs even when the S4-S5 linker is severed or removed in $K_V10.1$ (Lörinczi et al. 2015) or $K_V11.1$ (de la Pena et al. 2018). A thorough understanding of gating mechanisms in this family is also relevant in practical terms because members of the family are implicated in many pathological conditions, as is the case for Kv101 (Bauer and Schwarz 2018; Toplak et al. 2022), which makes these channels attractive therapeutic targets.

Although *KCNH* channels do not display domain-swapping in the transmembrane domains, they show extensive conserved intracellular domains where intersubunit interactions occur. The so-called eag domain in the N-terminus, formed by the PAS domain and PAS-Cap, interacts with the CNBHD (cyclic nucleotide-binding homology domain, see Fig. S1A) of the neighboring subunit, which is connected to the S6 through the C-linker. The four eag-CNBHD complexes form a ring in the intracellular side of the channel, connected to the gate via the C-linkers (Whicher and MacKinnon 2019; Whicher and MacKinnon 2016). Thus, there is domain-swapping within intracellular domains instead of the transmembrane segments (reviewed, e.g., in (Barros et al. 2020; Codding et al. 2020)). This arrangement makes the intracellular ring an excellent candidate to participate in the gating process, as it has been demonstrated for other channels, e.g.(Codding et al. 2020; James and Zagotta 2017; Nunez et al. 2020; Verkest et al. 2022). The first residues of the PASCap segment, although unresolved in the available structures of Kv10.1, occupy in Kv11.1 a space close to the S4-S5 linker and the C-linkers, suggesting its participation in transducing the movements of the voltage sensor to the intracellular ring (Wang and MacKinnon 2017; Stevens-Sostre et al. 2024). Indeed, the gating of *KCNH* channels is affected by manipulations of either the eag domain, the CNBHD, or the interaction between them (Stevens-Sostre et al. 2024; Malak et al. 2019; Whicher and MacKinnon 2019;

Codding et al. 2020; Codding and Trudeau 2019; Dai and Zagotta 2017; Dai et al. 2018; Gianulis et al. 2013; Ju and Wray 2006; Sahoo et al. 2012; Terlau et al. 1997). Furthermore, the interaction between the PAS domain and the C-terminus is more stable in closed than in open $K_V11.1$ (HERG) channels, and a single chain antibody binding to the interface between PAS domain and CNBHD can access its epitope in open but not in closed channels, strongly supporting a change in conformation of the ring during gating (Harley et al. 2021). Recent cryo-EM work revealed that the position of the voltage sensor in a polarized membrane would preclude the opening of the gate (Mandala and MacKinnon 2022). After relieving such an obstacle upon depolarization, a rotation of the intracellular ring would allow the helices at the bottom of S6 to dilate, opening the gate (Whicher and MacKinnon 2019; Whicher and MacKinnon 2016; Wang and MacKinnon 2017; Wynia-Smith et al. 2008). Moreover, cryo-EM data on $K_V10.2$ (which shows 76% identity with $K_V10.1$) reveals a pre-open state in which the transmembrane regions of the channel are compatible with ion permeation (the permeation path is dilated, like in open states) but the intracellular gate is still in the same conformation as in closed states (Zhang et al. 2023). Whether the difference between these two states depends on the rotation of the intracellular ring remains to be addressed.

The intracellular ring is also subject to modulation by factors external to the channel molecule. For example, ligand binding to the PAS domain can modify gating (Wang et al. 2020; Wang et al. 2023), explaining the complex effects induced by some inhibitors such as imipramine. The association of $K_V10.1$ with calmodulin (CaM), which efficiently inhibits the channel in the presence of Ca^{2+}, adds an additional level of complexity (Whicher and MacKinnon 2016; Schonherr et al. 2000). $K_V10.1$ has CaM binding sites at the N- and the C-termini (Gonçalves and Stühmer 2010; Schonherr et al. 1999; Ziechner et al. 2006). CaM presents two Ca^{2+}-binding lobes (N- and C-lobe) joined by a flexible helix. The N-lobe of CaM (Babu et al. 1985) binds to the N-terminal site in one channel subunit, while the C-lobe binds the C-terminal sites of the opposite subunit (Whicher and MacKinnon 2016), therefore linking two PAS/CNBHD pairs. It is plausible that his cross-linking of two segments of the ring impairs its rotation and can thus be the basis of the inhibitory action of CaM.

Yet, the mechanism coupling the movement of the voltage sensor and the rotation of the ring remains unsolved. A candidate to fulfill this function is the segment encompassing the first ten N-terminal residues, which, by analogy to Kv11.1, could interact with the distal end of S4 (Stevens-Sostre et al. 2024). Importantly, mutations in both the intracellular N- (Whicher and MacKinnon 2019) and C-terminal domains (Zhao et al. 2017) cause unexpected rectification or paradoxical activation by Ca-CaM instead of the normal inhibition seen in wild type (WT) (Lörinczi et al. 2016).

In this study, we provide a mechanistic explanation of the hallmarks of $K_V10.1$ gating and define the role of the intracellular ring using a combination of electrophysiology and mutagenesis, modeling, and

biochemical approaches. Channel variants with altered interaction between PASCap and CNBHD uncovered an open state in the mutants, different from the main open state in the WT. Unlike the canonical

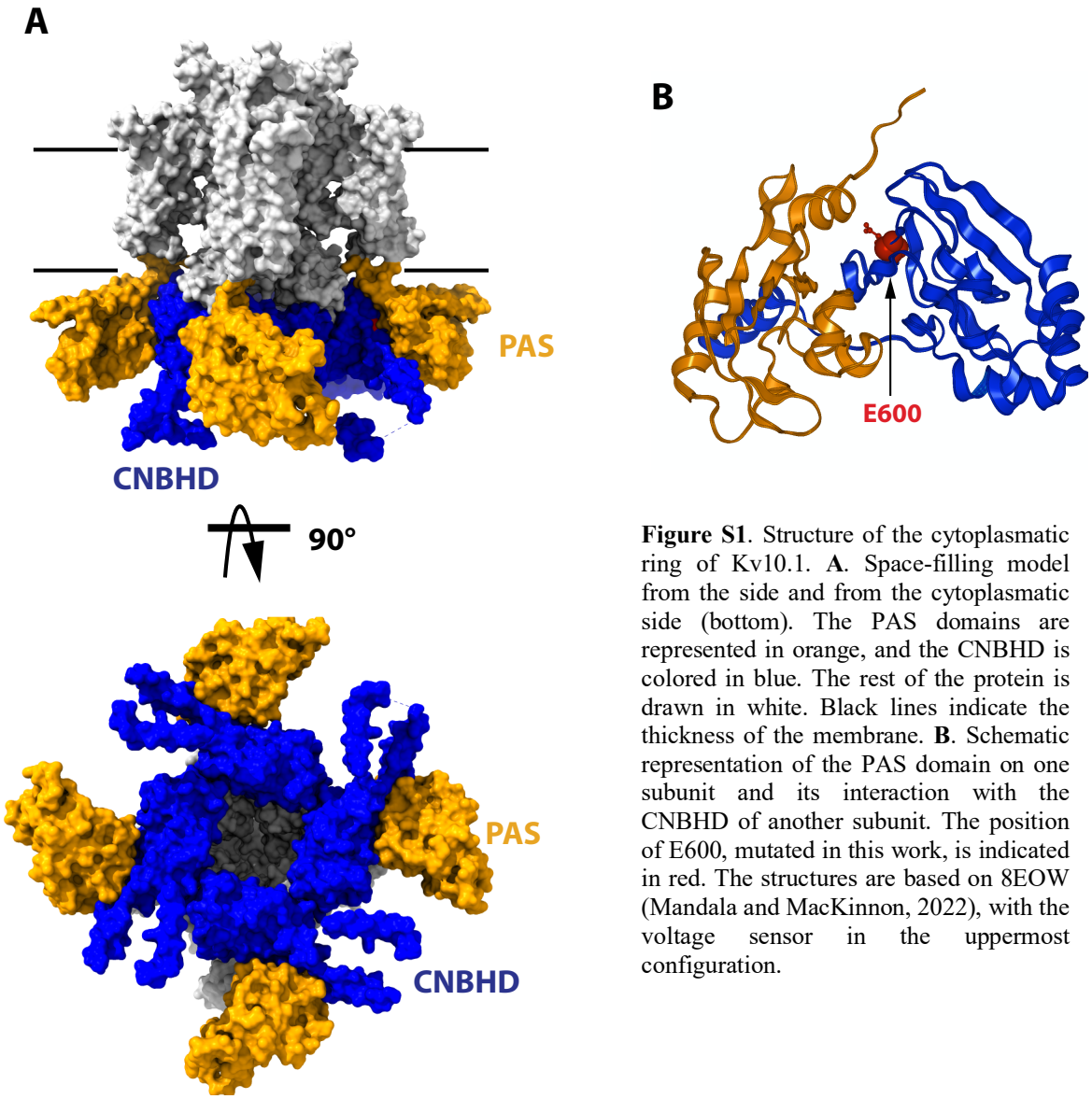

Figure S1. Structure of the cytoplasmatic ring of Kv10.1. **A**. Space-filling model from the side and from the cytoplasmatic side (bottom). The PAS domains are represented in orange, and the CNBHD is colored in blue. The rest of the protein is drawn in white. Black lines indicate the thickness of the membrane. **B**. Schematic representation of the PAS domain on one subunit and its interaction with the CNBHD of another subunit. The position of E600, mutated in this work, is indicated in red. The structures are based on 8EOW (Mandala and MacKinnon, 2022), with the voltage sensor in the uppermost configuration.

open state, the mutant-specific open state is not subjected to a flicker block and, therefore, gives rise to a larger macroscopic current. Because this state is best accessed from deep closed states (strong hyperpolarized membrane potential), it made the transition between the voltage sensor movement and the ring rotation visible, allowing the characterization of gating steps hidden in WT. Furthermore, access to the novel open state is promoted by the binding of CaM, thus explaining the paradoxical effects of CaM in mutant channels. We propose a model tightly constrained by data that can explain the main differential features of K_V10.1 gating.

Results

Disrupting the interaction between PASCap and CNBHD reveals a biphasic gating behavior.

The first N-terminal residues of $K_V10.1$ (PASCap (Morais-Cabral et al. 1998)) are prime candidates for transmitting voltage sensor motion to the intracellular domain based on crystal structures and interactions inferred from mutagenesis experiments. In particular, two residues at the bottom of S4 –H343 (Terlau et al. 1997) and D342 (Tomczak et al. 2017)– functionally interact with the initial N-terminus. The N-terminal PAS domain can then transmit mechanical cues to its C-terminal interaction partner CNBHD (Whicher and MacKinnon 2019; Whicher and MacKinnon 2016; Codding et al. 2020; Codding and Trudeau 2019; Mandala and MacKinnon 2022; Wang et al. 2020). To study $K_V10.1$ gating under perturbed intramolecular interaction, we deleted the PASCap domain (residues 2-25) and, in a more conservative approach, we examined the impact of a point mutation (E600R, Fig. S1B) reported to disrupt the PASCap-CNBHD interaction (Haitin et al. 2013) and which shows a behavior reminiscent of the PASCap deletion in its response to calmodulin (see below; (Lörinczi et al. 2016)). We then obtained the response of the mutants to discrete depolarizations to different potentials (-100 to +120 mV for 300ms) in *Xenopus* oocytes in the presence of 60 mM K^+ in the extracellular solution to follow deactivation behavior through tail currents.

Fig. 1A displays representative current traces of WT and the mutant channels. The threshold for activation was shifted towards hyperpolarizing values in both mutants, giving rise to inward currents at potentials that do not lead to the opening of WT channels. This shift is most evident in the biphasic conductance-voltage (GV) plots (Fig. 1B). The kinetics of activation (Fig. 1C) and deactivation (Fig 1E) of the mutants were also clearly distinguishable from WT. To facilitate the description of the results, we classified the responses into three categories depending on the stimulus amplitude: *weak* (-90 mV to -20 mV), *moderate* (-10 mV to +40 mV), and *strong* (+50 to +120 mV).

While the activation of WT currents does not accelerate dramatically with increasing depolarizations in the voltage range tested, the mutants activated much slower than the WT upon *weak* and *moderate* depolarizations, reaching activation kinetics similar to WT with *strong* ones, as can be observed in normalized traces (Fig 1C). To obtain a more quantitative estimation of the changes in activation velocity, we used the time required to reach 80% of the maximum current amplitude plotted against the stimulus voltage (Fig. 1D). ΔPASCap and E600R needed a much longer time than WT to activate at *weak* depolarizing potentials but were equally fast at membrane potentials larger than +50 mV.

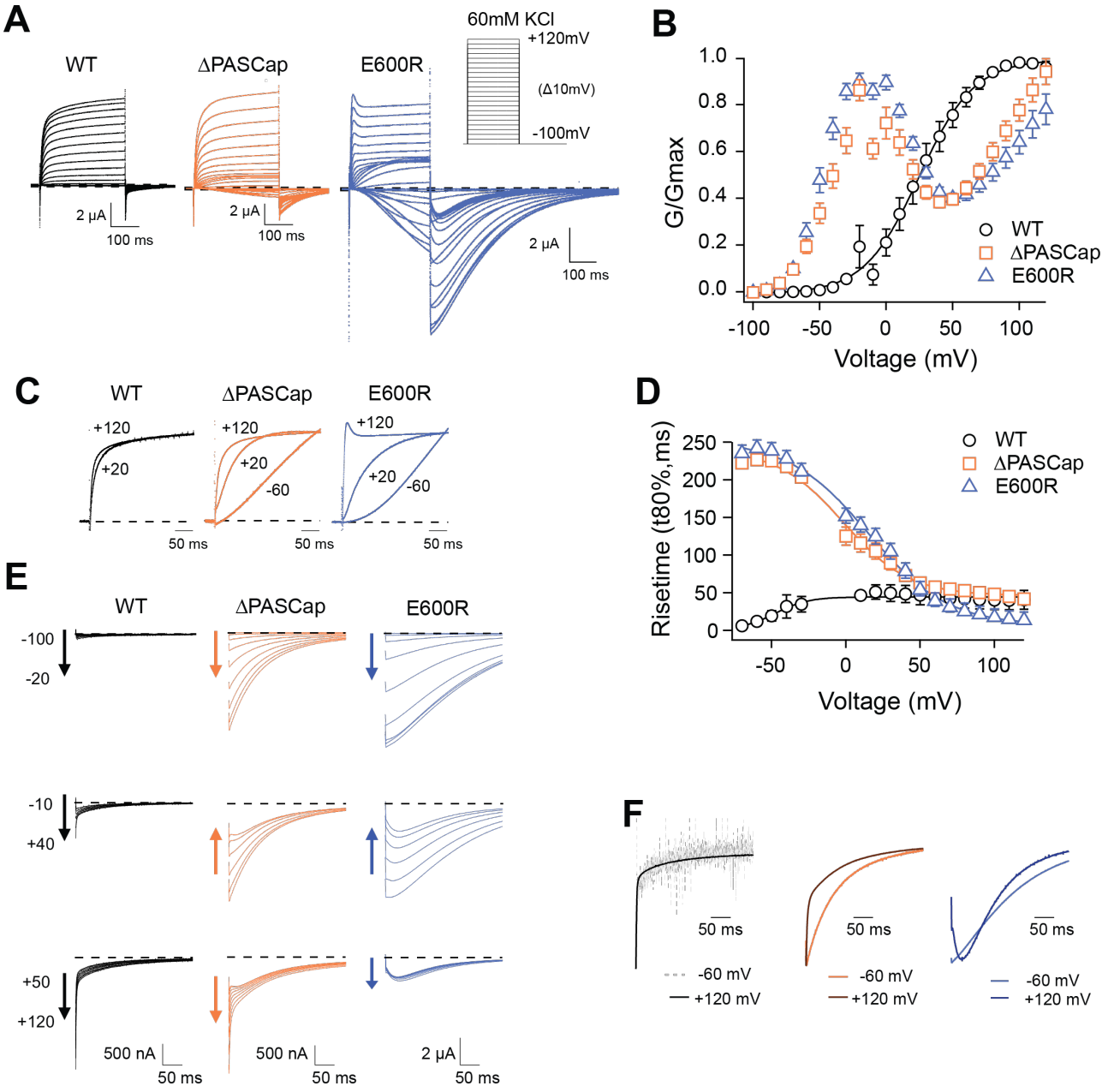

Figure 1. Characterization of ΔPASCap and E600R mutants. A. Raw current traces resulting from depolarizations between -100 and +120 mV in WT (black), ΔPASCap (orange), and E600R (blue). The dashed lines indicate zero current. The stimulus protocol is schematically depicted in the inset. The extracellular solution contained 60 mM KCl, 57.5 mM NaCl, 10 mM HEPES, 1.8 mM CaCl2, pH=7.4 **B**. GV plots corresponding to the three channel variants (colors as in A). (N: WT = 6, ΔPASCap = 7, E600R = 11; mean±SEM) **C**. Normalized traces to the indicated voltages to reveal the acceleration of activation with depolarization in the mutants. WT does not give rise to significant outward current at -60 mV. **D**. Rise time of ΔPASCap and E600R as a function of voltage (colors as in A). The activation is much slower than in WT up to +50 mV but reaches the speed of WT with stronger stimuli. **E**. Tail currents at -100 mV after depolarizations to potentials in the weak, medium, or strong range (up to down, see text for details). The arrows indicate the direction of the change in tail peak amplitude with increasing voltage. **F**. Normalized tail currents at -100 mV after depolarizations to the indicated voltages.

The deactivation (tail) kinetics changes with increasing depolarizations were more evident and more complex than changes in activation kinetics (Fig. 1E and 1F). For increasing test pulse potentials, the peak amplitude of ΔPASCap tail currents first increased progressively, then decreased at *moderate* values, and rose again after the range of *strong* depolarizations. E600R showed a similar pattern of tail amplitude, while the increase at *strong* potentials was less pronounced although still evident. Remarkably, both the tail amplitude and its decay kinetics underwent profound changes depending on the stimulus. While the kinetics of WT tail currents was the same across different potentials, showing the characteristically fast deactivation of $K_V10.1$, ΔPASCap deactivated slow- and monotonically at *weak* depolarizations, but a fast component started to become evident after *moderate* stimuli. The fast component dominated the process at *strong* depolarizations. For E600R, the deactivation after *weak* stimuli was also slow and accelerated after a rising phase in the *moderate* and *strong* depolarization range.

Due to the complex behavior of the tail currents, different equations would be needed to fit the tails of the various channels to extrapolate the amplitude to time zero. Hence, to calculate the macroscopic conductance, we simply used the current amplitude at the end of the depolarizing stimulus and divided it by the driving force calculated from the measured reversal potential (Fig. 1B). As already observed in the raw traces, the threshold for activation for both mutants was strongly shifted in the hyperpolarizing direction with respect to WT (-80 mV *vs.* -40 mV). Still, the most evident change was that both ΔPASCap and E600R displayed a biphasic GV in contrast to WT. *Weak* depolarizing pulses increased the macroscopic conductance of both mutants until a maximum at approximately +10 mV. With further depolarizations, the conductance initially declined to rise again in response to *strong* depolarizations. This finding matches the changes in amplitude of the tail currents, which, therefore, probably reflect a true change in overall conductance. A similar behavior has been mentioned for related (Whicher and MacKinnon 2019) or unrelated mutations (Zhao et al. 2017) affecting the intracellular domains. However, the reasons for this phenomenon have not been investigated. We thus aimed to understand the molecular mechanisms underlying the biphasic GV.

The biphasic GV is described by two sigmoidal components corresponding to a two-step gating mechanism.

One possible explanation for the biphasic behavior could be the coexistence of two separate channel populations with different kinetics, amplitude, and voltage dependence. This seems unlikely because the shape of the GVs was consistent in all our recordings, as evidenced by the small error bars (Fig. 1B) despite the variability intrinsic to the oocyte system. Alternatively, each channel could have two open states, and the rectification observed between the two components could represent a transition from one state to the

other. Indeed, an equation that reflects the two components and a transition between them (Equation 4; see Methods) described the behavior of the GV of both mutants accurately (Fig. 2A). Representative current traces are shown in (Fig.1A and Fig. 2A, C).

With the available structural information in mind, the two components could represent sequential access to two open states (from here on, O_1 and O_2) through separate gating steps that differentially involve the sensor movement and ring rotation (Tomczak et al. 2017; Whicher and MacKinnon 2019; Mandala and MacKinnon 2022).

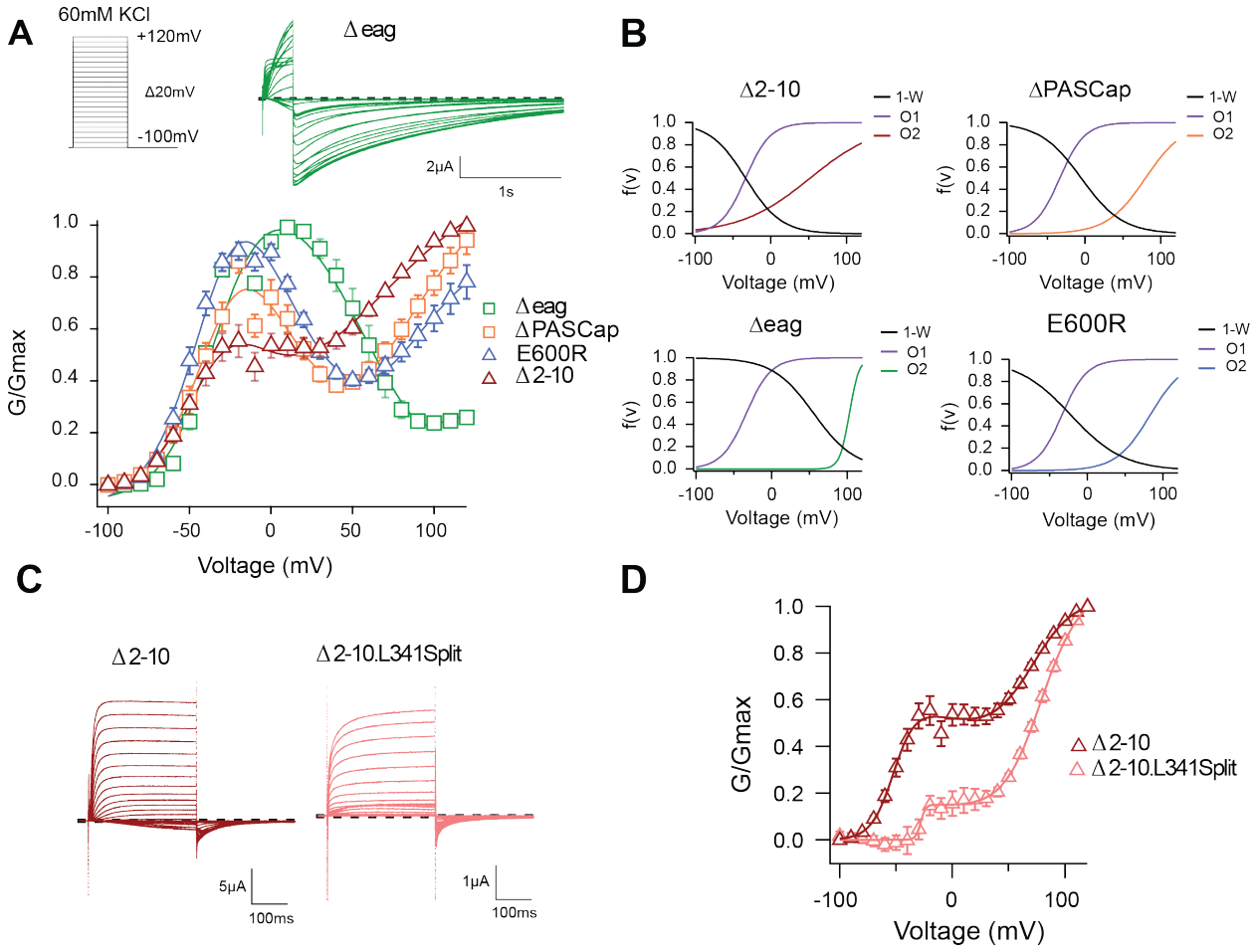

Figure 2. The biphasic GV corresponds to two sequential events. A. The GV of all tested mutants show biphasic behavior. (N: Δ2-10 = 6, ΔPASCap = 7, Δeag = 7, E600R = 11; mean±SEM). All are well described by *Eq. 4* in a global fit with fixed parameters for the first component. **B**. Distribution of the three components used for the fits as a function of voltage. **C**. A discontinuous form of Δ2-10 shows attenuated biphasic behavior. **D**. GV plots of Δ2-10 and Δ2-10.L341Split (N: Δ2-10 = 6, Δ2-10.L341Split = 5; ±SEM). Split fitted using *Eq. 4*. The dashed lines in **A** and **C** indicate zero current. The stimulus protocol is schematically depicted in the inset in **A**. The extracellular solution contained 60 mM KCl.

To test if the ring underlies one of the two gating steps, we tested the behavior of additional N-terminal deletions of increasing length (Δ2-10, 2-25 for ΔPASCap, and 2-135 for Δeag), expected to disrupt the ring integrity more and more. A biphasic GV was observed in all these mutants (Fig. 2A). The V_{half} value of the first component was very similar across mutants. In contrast, the second component showed different thresholds. We then performed a global fit using equation 4, where we linked the parameters of the first components (Vh_1, K_1) across mutants and allowed the parameters for the second component (Vh_2, K_2, A_2) and the transition (Vh_3, K_3) to vary (Table S1, Fig. 2B). The global fit accurately described the behavior of the GV in all mutants (Fig. 2A).

	Δ2-10	ΔPASCap	Δeag	E600R
A_0	-0.052	-0.054	-0.067	-0.091
A_1	1.78	1.78	1.32	2.99
Vh_1	-33.57	-33.57	-33.57	-33.57
K_1	16.38	16.38	16.38	16.38
A_2	1.31	1.18	0.25	0.99
Vh_2	51.63	79.63	102.70	83.04
K_2	46.05	25.38	6.41	22.51
Vh_3	-33.47	-5.16	55.52	-21.93
K_3	23.47	27.12	27.01	34.9

Table S1. Parameters of a global fit that linked the first component of the biphasic response.

The global fit results indicate that the first component is conserved across mutants. In contrast, the second component occurs at progressively more depolarized potentials for increasingly larger N-terminal deletions and when the structure of the ring is altered through disruption of the interaction between N- and C-termini (E600R). Thus, the underlying gating events can be separated into two steps: The first gating step involves only the voltage sensor without engaging the ring and leads to a pre-open state, which is non-conducting in the WT but conducting in our mutants. The second gating event operates at higher depolarizations, involves a change in the ring, and leads to an open state both in WT and in the mutants.

To test this hypothesis, we compared the behavior of Δ2-10 and Δ2-10.L341Split, a channel lacking a covalent connection between the sensor and the pore domain (Tomczak et al. 2017), hence decoupling residues downstream S4 (in this case starting from 342) from the movement of the sensor. This decoupling would minimize the action of the displacement of the voltage sensor on the pore domain but would not necessarily affect the subsequent ring rotation. As predicted, compared to Δ2-10, Δ2-10.L341Split showed

a significant reduction in the first component of the biphasic GV (Fig. 2C, D). This indicates that the coupling of the voltage sensor motion to the entry into O_2 does not require a continuous S4-S5 linker. If, in non-split mutants, the upward transition of S4 allows entry to O_1, it is reasonable to assume that the movement is not transmitted the same way in the split and the transition into O_1 is less probable. The observation that, in the split, entry into O_1 requires higher depolarization and appears to be less likely, suggests that downstream of S4 (beyond position 342), there is a mechanism to convey S4 motion to the gate of the mutants.

Activation of WT $K_V10.1$ channels (best studied for the *Drosophila* form *eag*) drastically slows down in the presence of extracellular divalent cations that bind to the voltage sensor (Silverman et al. 2000; Tang et al. 2000), e.g., Mg^{2+}, Ni^{2+}, Co^{2+}, and Mn^{2+}, but not Ca^{2+}. Strikingly, the degree of deceleration correlates with the ions' hydration enthalpy, suggesting that the ion might unbind during activation (Terlau et al. 1996). We chose to study the impact of Mg^{2+} on the kinetics and voltage dependence of activation (Fig. 3) in the mutant Δeag, which shows the most significant separation between the two conductance components.

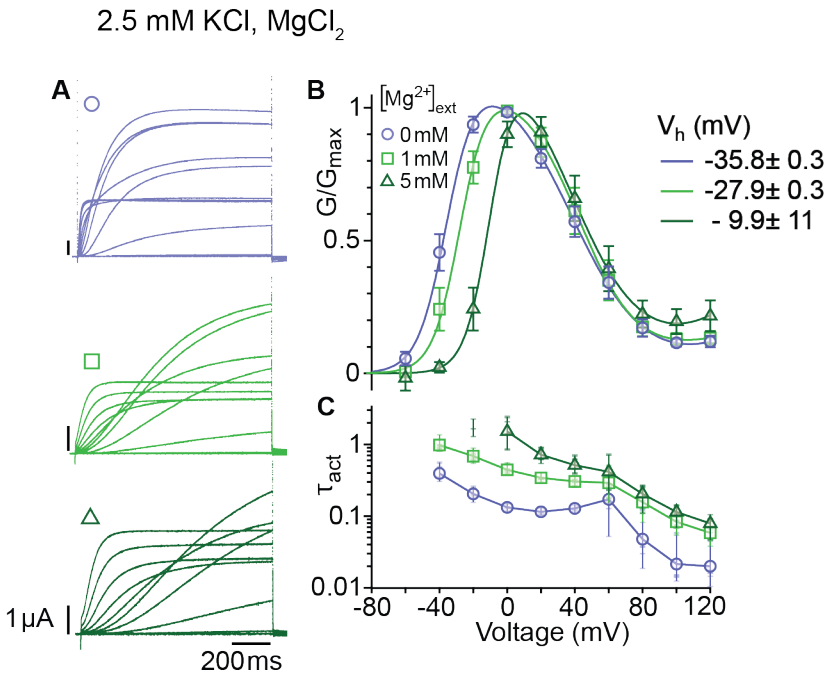

Figure 3. Mg^{2+} induces a shift of the first component in the depolarizing direction. A. Raw current traces from oocytes expressing Δeag channels in response to depolarizations from a holding potential of -100 mV to voltages between -100 and +120 mV in the presence of 0, 1 or 5 mM $MgCl_2$ in the external solution (legend in B). Scale bars are 1µA and 200 ms. **B**. Average GV plots (with SEM) obtained under the same conditions from n=6, 6, and 5 recordings (0, 1, and 5 mM $MgCl_2$). The V_{half} of the first component shifts from -35.8 mV in the absence of extracellular Mg^{2+} to -27.9 and -9.9 mV in 1 mM and 5 mM $MgCl_2$. **C**. Time constants of the early activation show the decelerating effect of Mg^{2+}. Symbols depict averages, vertical lines the range and horizontal lines individual experiments. For voltages where conductances or time constants could not be reasonably estimated no data are displayed. The recordings were performed in an external solution containing 115 mM NaCl, 1.8 mM $CaCl_2$, 2.5 mM KCl, 10 mM Hepes pH 7.2, and the indicated concentrations of $MgCl_2$,

Mg^{2+} slowed the activation of the channel at all depolarizations, affecting entry to both open states. This result suggests that Mg^{2+} also slows the voltage sensor motion that controls access into the second open state. In addition, the voltage dependence of activation was shifted by approximately 25 mV to more depolarized voltages. This is in line with deep deactivated states bound to Mg^{2+} and requiring stronger depolarization to exit them. Interestingly, the transition from the first to the second component of the GV plot seems unaffected by the extracellular divalent binding, which could be expected if the transition occurs in the cytoplasm.

Steady-state voltage dependence and activation kinetics are consistent with two open states (O_1 and O_2) with different conducting behavior.

Thus far, our results are compatible with two different open states in the mutants. The first open state, the mutant-specific O_1, would dominate at *weak* depolarizations and deactivate slowly, with tail current decay time constants of tens of milliseconds. In contrast, mutant and WT channels would reach the second open state (O_2) at strong depolarizations and deactivate more rapidly, with a few milliseconds or less time constants. A critical test of this hypothesis is the application of more complex voltage stimuli that drive the system to a non-equilibrium state of high O_1 occupancy. This might be achieved by deactivation periods of around 10 ms, just long enough to remove most channels from O_2 but sufficiently brief to maintain the occupancy of O_1. For simplicity, we used depolarization periods of the same duration and tested whether a 300 ms series of activating and deactivating 10 ms pulses could accumulate channels in a high conducting state O_1.

For WT (Fig. 4A), alternating between -80 and +80 mV resulted in a smaller amplitude than a constant stimulus to +80 mV, just as expected for a system with a single open state and a monotonic voltage dependence of activation. Moreover, WT's rapid deactivation resulted in near-complete deactivation during every cycle.

In E600R, in contrast, the current amplitude during activating pulses increased steadily from cycle to cycle. Ultimately, the current amplitude exceeds that obtained with a constant +80 mV pulse (Fig. 4A). Because the deactivation of this mutant is much slower and occurs at more negative potentials than that of WT (see Fig. 1 and 2B), there was no noticeable deactivation during the -80 mV episodes. In addition, the tail current after the alternating stimuli had a larger amplitude than the one after a continuous pulse and decayed mostly as one component. All those observations are consistent with an accumulation of channels in O_1. A similar behavior was detected with ΔPASCap (Fig. 4B), albeit within a different voltage range, as could be predicted from the different voltage dependence of the transition between states (Fig. 2B). Again,

alternating pulses resulted in larger current amplitudes and less complex tail current as compared to a single long pulse (Fig. 4B).

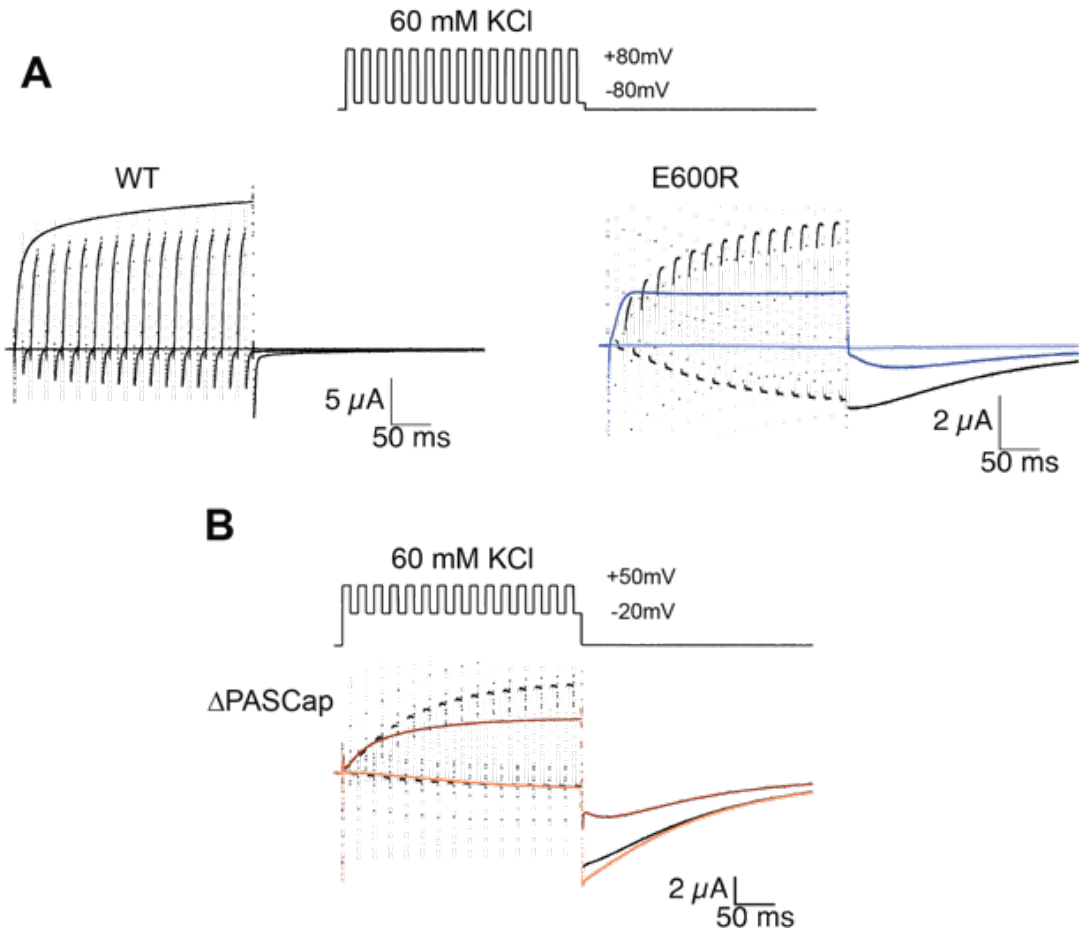

Figure 4. Alternating stimuli reveal larger macroscopic conductance for O_1. A. Alternating potential between -80 and +80 mV in the WT results in current amplitudes that are smaller than those during a sustained stimulus (Upper left traces). In contrast, E600R gave rise to larger currents when the stimulus was intermittent and too short to allow occupancy of O_2 (upper right). Current traces in response to a sustained stimulus are shown in blue (dark trace +80 mV ; light trace is -80 mV) **B**. The effect was qualitatively similar for ΔPASCap, which consistently gave rise to larger current upon oscillating stimuli between -20 and +50 mV than during a constant pulse to +50 mV. Current traces in response to a sustained stimulus are shown in orange (dark trace +50 mV ; light trace is -20 mV). The stimulus protocol for A and B is schematically depicted in the inset. The extracellular solution contained 60 mM KCl.

Single channel recordings reveal two distinct voltage-dependent behaviors in ΔPASCap.

A larger current amplitude in O_1 can be due to a larger single-channel conductance or a different open probability. We performed single-channel recordings in membrane patches excised from oocytes expressing the ΔPASCap mutant to distinguish between these two possibilities. To limit the possible contamination by other channels, we measured the activity in outside-out patches with K^+ as the only cationic charge carrier on the cytoplasmic side (see Methods), rendering a theoretical Nernst equilibrium potential for K^+ of -93.77 mV and -4.69 mV for Cl^-. We only considered channels producing outward currents at -60 mV, ruling out Cl^- contamination. In such patches, we detected K^+ current during single-channel openings that typically lasted several milliseconds upon weak depolarizations but could rarely be resolved at strong depolarizations (Fig. 5A). Such behavior was never detected in uninjected oocytes. The activity in the patches was silenced by the addition of 100 µM astemizole, providing robust evidence that the activity is the result of the expression of ΔPASCap.

To characterize the activity in a quantitative way, we performed series of sweeps where the patch was held at -100 mV for 10 s, depolarized to +10 mV for 2.5 s, held again at -100 mV for 5 s, and finally depolarized to +40 mV for 2.5 s. The procedure was repeated tens of times on each patch, and representative traces are shown in Fig 5B. At +10 mV, we detected openings lasting up to hundreds of milliseconds, while the dwell times were much shorter at +40 mV. In some cases, openings of the two classes were observed in the same sweep, with the long openings preferentially preceding the shorter ones. Any transition from short openings to long openings (or back) always involved a longer intermediate close time, indicating that the channel travels between the two states through one or more closed states without a direct link between the two open states.

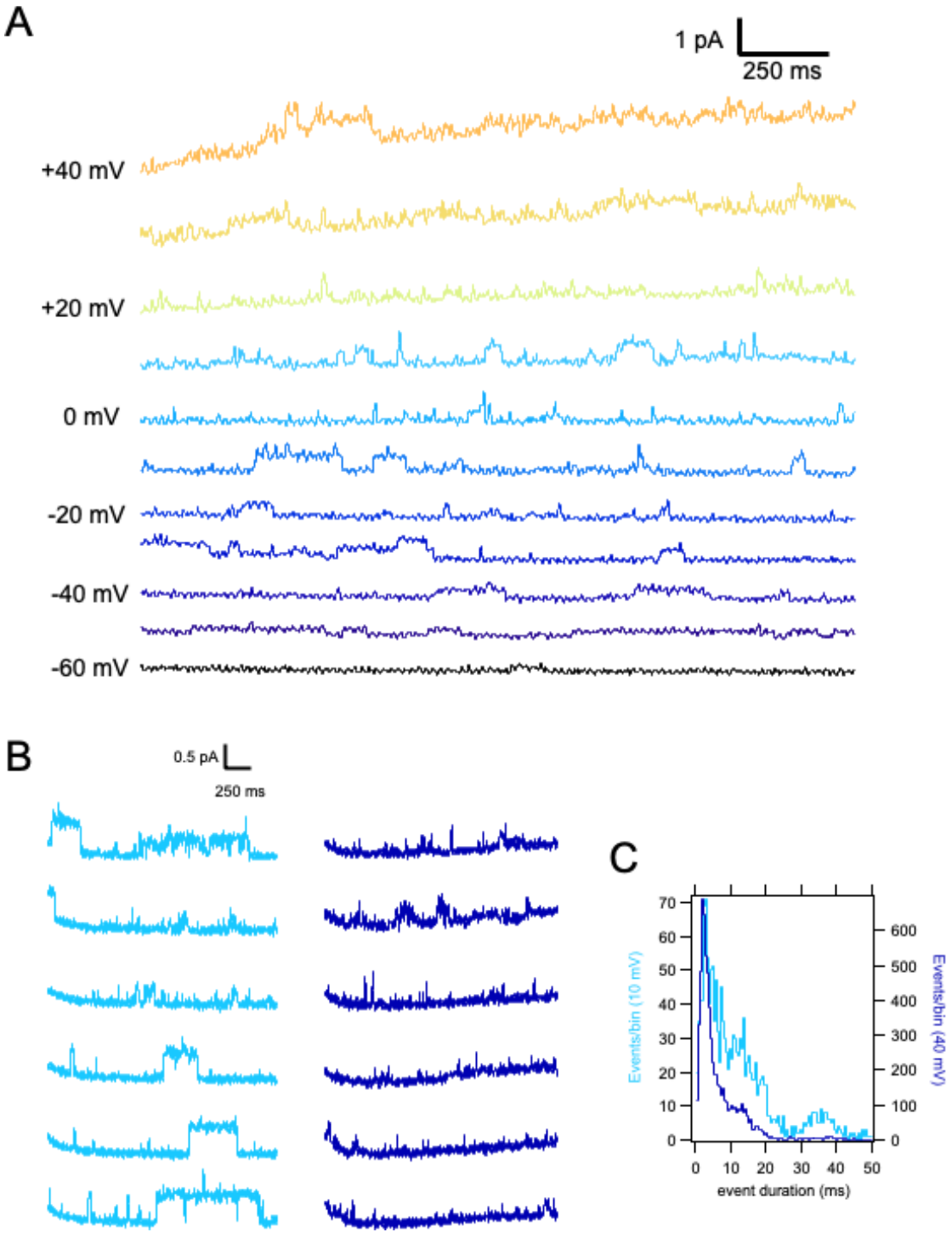

Figure 5. Single ΔPASCap channels reveal longer open times at moderate depolarizations. A. representative current traces at the indicated voltages obtained from a holding potential of -100 mV. **B**. Comparison between traces obtained at +10 mV (light blue) and +40 mV (dark blue). The time spent in the open state is much longer at +10 mV. **C**. Open time distribution for events shorter than 50 ms obtained from currents in an experiment like the one depicted in B, (100 stimuli at each potential).

Deep-closed states favor access to O_1

A hallmark of $K_V10.1$ gating is the change in activation kinetics in dependence on the pre-pulse potential reminiscent of (and commonly named) the Cole-Moore Shift (Cole and Moore 1960; Hoshi and Armstrong 2015). Hyperpolarized potentials drive the channel into deep closed states, which delays and decelerates activation (Ludwig et al. 1994). This is well described by a model with four identical, independent transitions of the voltage sensor (Schonherr et al. 1999) and is compromised by N-terminal deletions (Whicher and MacKinnon 2019). To test the behavior of our mutants concerning this property, we applied a series of 5s-long conditioning pulses with voltages ranging from -160 mV to -20 mV, followed by a test pulse to +40 mV in the absence of external Cl^-. The activation kinetics, quantified by the time to 80% of the maximum current, showed a strong pre-pulse dependence in WT, ΔPASCap, and E600R, with much larger rise times in both mutants (Fig. 6B).

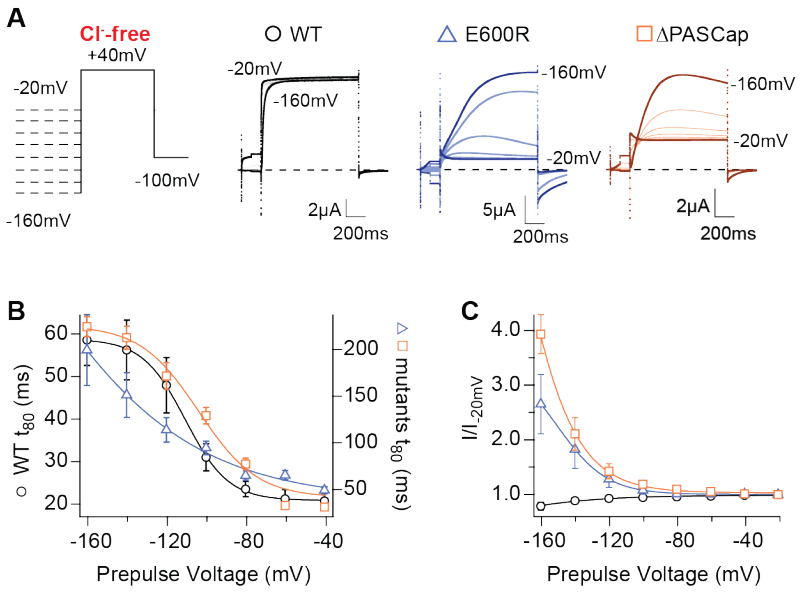

Figure 6. Hyperpolarization promotes access to a large conductance, slowly activating open state. A. Raw current traces in response to the stimuli depicted in the scheme. **B**. The rise time to 80% of the maximal current during the depolarizing stimulus is plotted *vs*. prepulse voltage (N: WT = 7, ΔPASCap = 9, E600R = 8; mean±SEM). Although the activation is much slower for both mutants (note the different y axis for the mutants), they retain a strong dependence on the prepulse potential. **C**. Normalized end-pulse current (I/I_{-20}) is plotted *vs*. prepulse voltage (N: WT = 10, ΔPASCap = 8, E600R = 8; mean±SEM). The amplitude of the current at +40 mV increased markedly when the holding potential was below -100 mV in the mutants, while the amplitude in WT changed only marginally. The dashed lines indicate zero current. The stimulus protocol is schematically depicted in the inset. A 5s pre-pulse was applied, of which only the initial and last 100ms were recorded. The chloride-free extracellular solution contained 115 mM Na-methanesulfonate, 2.5 mM KOH, 10 mM Hepes, 1.8 mM $Ca(OH)_2$, pH=7.2.

In the mutants, not only activation kinetics but also current amplitude was substantially affected by hyperpolarizing pre-pulses. With respect to the -100 mV pre-pulse potential, the current starting from a -160 mV pre-pulse increased in ΔPASCap by a factor of 3.93 ± 0.36 and in E600R by a factor of 2.65 ± 0.54. In contrast, WT current amplitude was not significantly affected (Fig. 6A, 6C). Such increases in amplitude are often related to augmented channel availability due to voltage-dependent recovery from inactivation. Still, although under some conditions, a decrease in outward current can be observed during the stimulus (see, e.g., traces of E600R in Fig. 1 and traces in Fig. 6), we never detected in any mutants cumulative inactivation after repeated depolarization, as depicted, e.g., in Fig. 4. Transition from a conducting to a non-conducting state while the depolarization persists is the definition of inactivation. We nevertheless prefer to refer to the non-conducting states as "closed" rather than "inactivated", because O_1 is non-conducting (or not accessed) in the WT, and therefore, the subsequent states cannot be considered inactivated. The state resulting from the flickering block from O_2 is arguably inactivated, but such events are commonly not defined as inactivated because of their unstable nature.

In the absence of canonical inactivation, the prepulse-dependent current increase at +40 mV could be related to changes in the relative occupancy of the open states. We hypothesized that the open state O_1, which produces larger macroscopic currents, might be more accessible after a hyperpolarization. The current decay after the peak (Fig. 6A), especially in ΔPASCap, also indicates a transient phenomenon. To map the voltage dependence of this effect more comprehensively, we next compared the effect of hyperpolarized pre-pulse on currents elicited at different test potentials.

We tested the effect of pre-pulse potentials (-160 and -100 mV) on IV protocols in the absence of Cl^-. Compared to a -100 mV pre-pulse, -160 mV clearly potentiated the first component of ΔPASCap and E600R biphasic IV (Fig. 7A and 7B).

If the hyperpolarizing potentials facilitate the access to O_1 by driving the channel into deep closed states, then impairing the access to these states will reduce the component corresponding to O_1 in the GV. The mutation L322H, located in the S4 segment, limits access to deep closed states in WT channels (Schonherr et al. 1999). We introduced this mutation in the context of ΔPASCap and E600R. Representative current traces obtained from $\Delta PASCap^{L322H}$ and $E600R^{L322H}$ are shown in Fig. 7C and D. Both mutants showed drastic attenuation in the first component of the biphasic GV compared to the parental channels. The tail currents of $\Delta PASCap^{L322H}$ and $E600R^{L322H}$ did not show rectification. They presented homogenous kinetics at all potentials, indicating that reducing the access to deep closed states also reduces the occupancy of O_1.

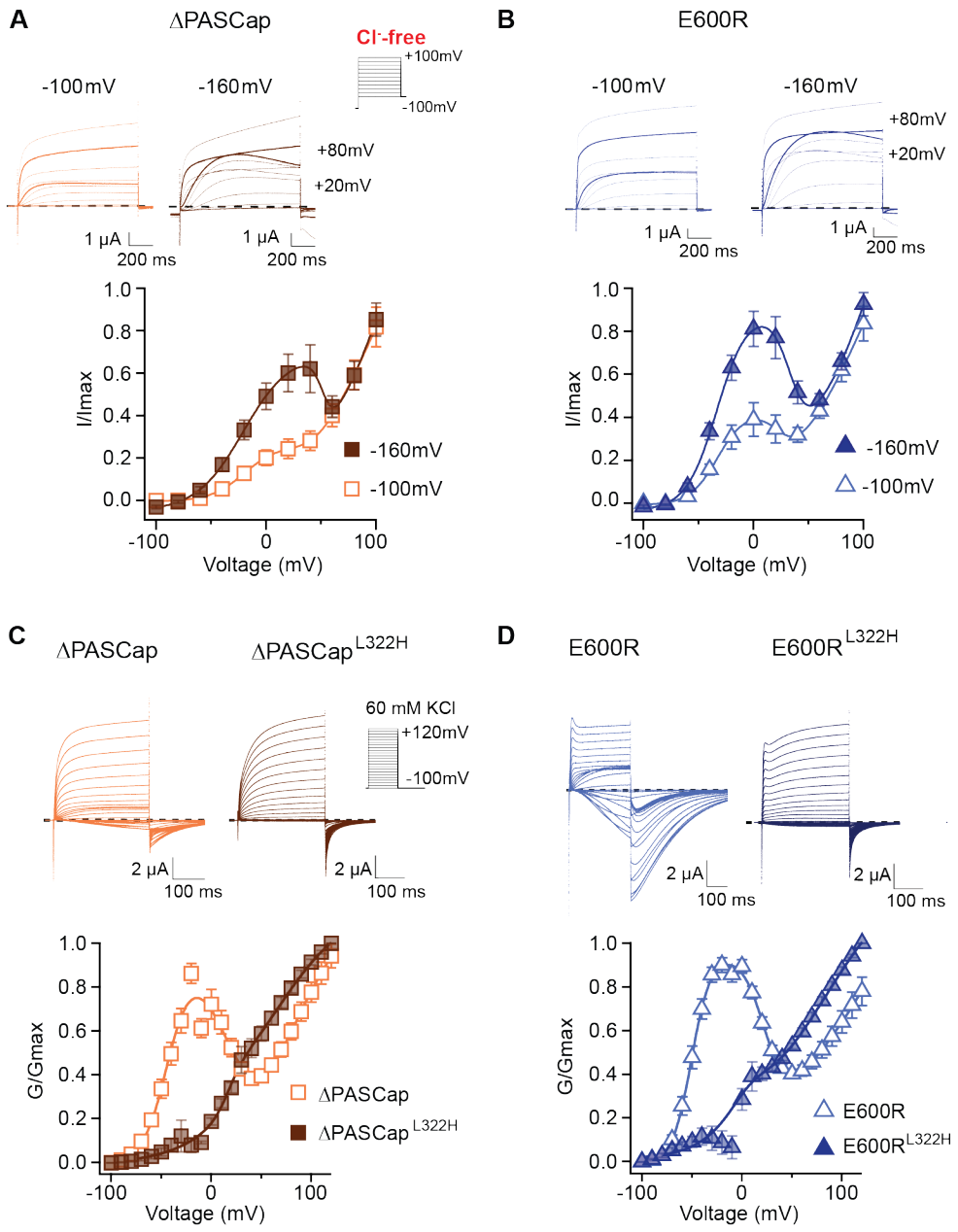

Figure 7. Deep closed states facilitate access to O_1. A, B. Conditioning pulses to -160 mV potentiated the first component and hence the biphasic behavior of the I/V relationships for ΔPASCap (A) and E600R (B). (N: ΔPASCap = 7, E600R = 6; mean±SEM) The stimulus protocol is schematically depicted in the inset. A 5s prepulse to -160 or -100 mV was applied, which is not shown in stimulus cartoons or current traces. The extracellular solution did not contain chloride. **C, D**. A mutation known to impair access to deep closed states (L322H) largely removes the initial phase of the GV curves for ΔPASCap (C) and E600R (D). (N: ΔPASCap = 7, $\Delta PASCap^{L322H}$ = 6, E600R = 11, $E600R^{L322H}$= 7; mean±SEM). Recordings were performed in a solution containing 60 mM KCl. The stimulus protocols are depicted schematically in the insets. The dashed lines indicate zero current.

Ca^{2+} Calmodulin stabilizes O_1

The available cryo-EM structures show $K_V10.1$ in a complex with Ca^{2+}-CaM and therefore in a non-conducting state, as it is well established that binding a single Ca^{2+}-CaM inhibits the current through WT channels (Schonherr et al. 2000; Ziechner et al. 2006). In stark contrast, increasing intracellular Ca^{2+} has been reported to potentiate ΔPASCap and E600R current amplitudes (Lörinczi et al. 2016). In the light of the results described above, this seemingly paradoxical behavior of mutants could be explained if Ca^{2+}-CaM binding restricts the access to the WT-like open state O_2 while facilitating access to O_1, which gives rise to larger currents and is not visible in WT channels. Therefore, we predicted that Ca^{2+}-CaM binding would potentiate the first component of the biphasic IV in the mutants.

To test this, we induced a rise in cytosolic Ca^{2+} using the ionophore ionomycin and inducing release from the stores with thapsigargin (both 5µM) (Lörinczi et al. 2016). Because the increase in intracellular Ca^{2+} is transient and reverts after approximately 150s (see Supp. 1 to Fig. 8), and our protocols with discrete voltage pulses require a long time to complete, we used a 5s voltage ramp from -120 to +100 mV repeated every

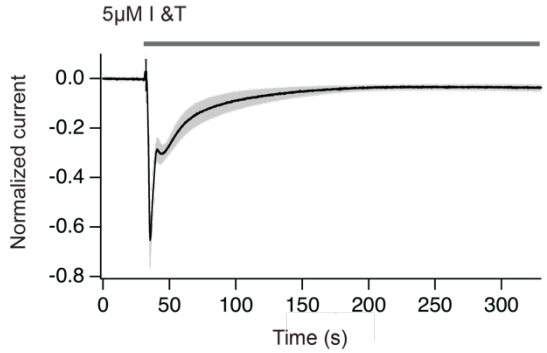

Supplement 1 to Figure 8. Chloride currents obtained upon treatment with ionomycin plus thapsigargin. The increase in cytosolic Ca^{2+} translates in a Cl^- current that can be used to estimate the amplitude and duration of the Ca^{2+} increase. Notice that Ca^{2+} returns to basal levels in approximately 150 s. The gray area indicates SEM. N=9

30s for 300s. The currents were recorded in Cl^--free extracellular solution to avoid confounding effects of the endogenous Ca^{2+}-dependent Cl^- channels. The results of representative experiments on ΔPASCap and E600R are shown in the upper left panels of Fig. 8A and B, respectively. 60 s after ionomycin/thapsigargin application, a marked potentiation of the current amplitude was observed, and the response to the ramp became linear. The current amplitude declined over the following 300s, and the biphasic IV characteristics partly recovered. The speed and extent of recovery were higher for ΔPASCap than E600R; after 150s, the first component recovered by 39.84± 6.35% for ΔPASCap and 11.84±3.07% for E600R. This recovery time course matches that of the changes in cytoplasmic Ca^{2+} and agrees with the results obtained by Lörinzi et al. for constant pulses (Lörinczi et al. 2016). The magnitude of potentiation and change in IV shape was homogeneous enough among oocytes to allow averaging of the normalized current in all experiments (Fig. 8A and B, lower panel). The changes in slope can be easily observed in the corresponding first derivative of the normalized IV as a function of voltage shown in Supp. 2 to Fig. 8.

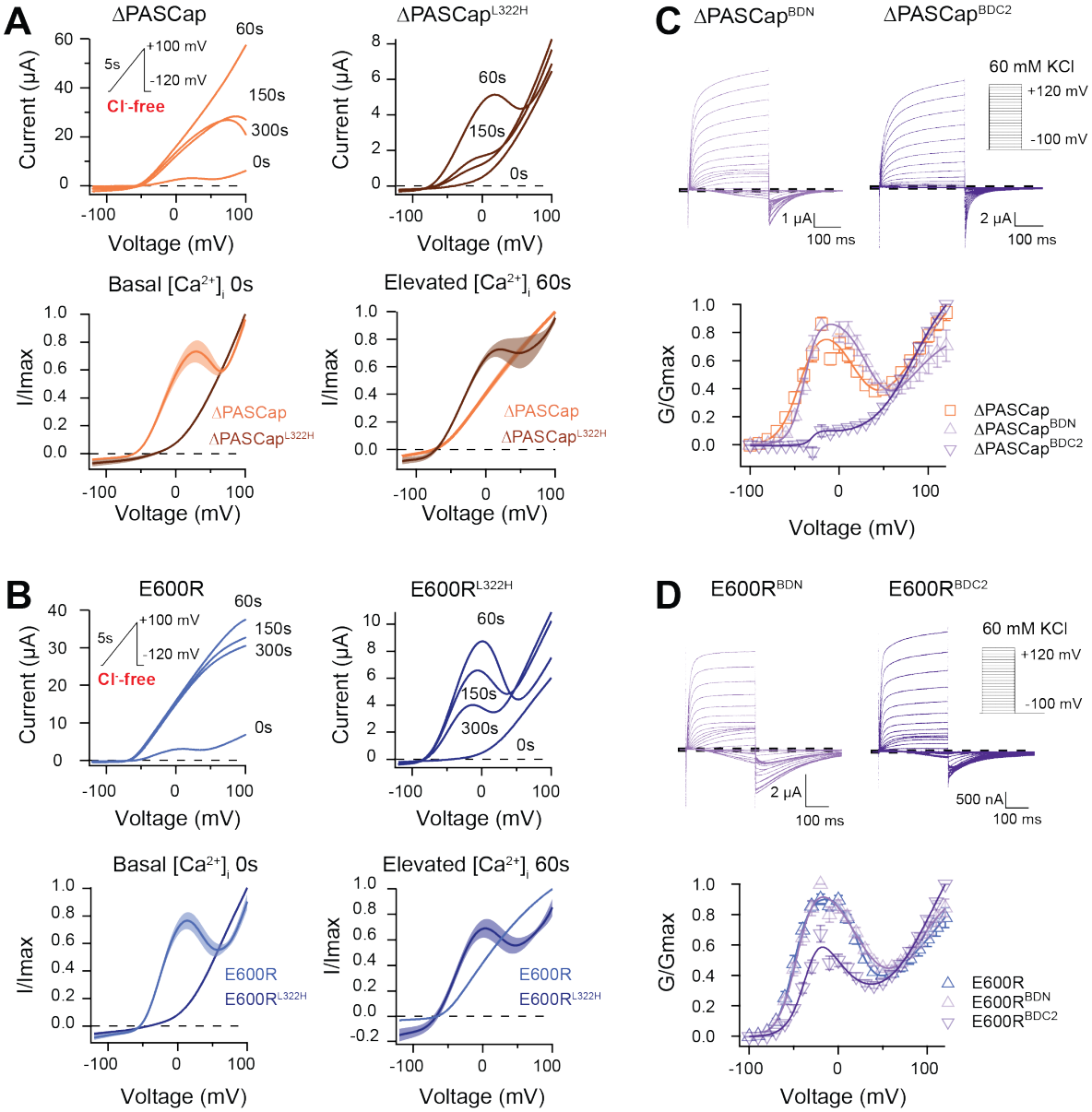

Figure 8. CaM stabilizes O_1. A. A transient rise in intracellular Ca^{2+} using 5μM ionomycin and thapsigargin increases ΔPASCap current amplitude (in the absence of external chloride) and the IV relationship becomes linear (upper left traces). The same treatment in a channel carrying a mutation (L322H), reducing access to deep closed states, results in the appearance of a biphasic IV upon Ca^{2+} rise (upper right traces). The lower traces represent the average normalized response comparing 0 and 60s. (ΔPASCap, light trace, N = 8, $\Delta PASCap^{L322H}$, dark trace, N= 5; the shadowed area indicates SEM). **B**. E600R behavior is comparable to ΔPASCap. Average normalized traces (E600R, light trace, N = 10; $E600R^{L322H}$, dark trace, N = 11; the shadowed area indicates SEM) are represented in the lower panel. The ramp protocol for A and B is schematically represented in the inset. The extracellular solution contained 2.5 mM K^+ and no chloride. The dashed lines indicate zero current level. **C**. Mutation of the C-terminal CaM binding domain (BDC2) in ΔPASCap strongly reduces the first component of the biphasic GV, while deletion of the N-terminal binding site (BDN) did not have any effect (N: ΔPASCap = 7, $\Delta PASCap^{BDN}$ = 7, $\Delta PASCap^{BDC2}$ = 7; mean ± SEM). **D**. The reduction of the first component in E600R when the C-terminal CaM binding site is mutated is also present but less intense. (N: E600R = 11, $E600R^{BDN}$ = 9, $E600R^{BDC2}$ = 11; mean±SEM). The experimental protocols for C and D are represented in the insets. Currents were recorded in the presence of 60 mM KCl. The dashed lines indicate zero current level.

The changes in amplitude and kinetics in response to rising intracellular Ca^{2+} support our hypothesis that Ca^{2+}-CaM stabilizes O_1, possibly by driving the channels to deep closed states (Figs. 7 and 8), which would result in smaller currents in WT and larger currents in mutants with access to O_1. We, therefore, predicted that forcing the channels to deep closed states using Ca^{2+}-CaM could restore access to O_1 in the channels with restricted access to deep closed sates $\Delta PASCap^{L322H}$ and $E600R^{L322H}$. This was tested with the approach described above, increasing intracellular Ca^{2+} while recording a repeated ramp protocol in $\Delta PASCap^{L322H}$ and $E600R^{L322H}$. As seen in the representative traces in the upper right panels in Fig. 8A and B, we observed a notable increase in current 60 s after Ca^{2+} rise, limited to *moderate* potentials, which results in a biphasic behavior resembling that of the ramps in the parental mutants in the absence of Ca^{2+}. For both mutants, the IV returned to a linear shape after 300s. Consistent with the observations for ΔPASCap and E600R, $\Delta PASCap^{L322H}$ exhibited faster recovery than $E600R^{L322H}$. Traces normalized to the maximum current and averaged are shown in Fig. 8A and B (lower panel). The respective first derivatives are shown in Supp. 3 to Fig. 8.

To further explore the role of CaM, we introduced mutations to preclude CaM binding at the N-terminal (F151N L154N) and C-terminal (F714S F717S) binding sites. We tested the behavior of these mutants (termed BDN and BDC2) in the context of ΔPASCap and E600R constructs (Fig 8C and D) under conditions of basal intracellular Ca^{2+} concentration. $\Delta PASCap^{BDN}$ showed a GV relationship like ΔPASCap. In contrast, $\Delta PASCap^{BDC2}$ lost its biphasic behavior. In the case of E600R, mutation of the C-terminal binding site ($E600R^{BDC2}$) showed attenuation of the first component of the GV, although not complete. The attenuation of the first component when binding of CaM to its C-terminal binding site is disrupted supports our hypothesis that Ca^{2+}-CaM stabilizes O_1. The significance of CaM for the mutants seems different. CaM might be crucial for stabilizing O_1 in ΔPASCap while less critical in E600R.

These results opened the possibility that the biphasic behavior is due to two coexisting populations of channels, depending on CaM binding at rest. We considered this possibility, but we find it is unlikely because i) the behavior of the mutants is very homogeneous among oocytes, in which resting Ca^{2+} is very variable; it can be as high as 400 nM (Busa and Nuccitelli 1985), although ten times lower concentrations have also been reported (Parker et al. 1996) and ii) two independent populations of channels would not explain the rectification or the voltage-dependent transitions during short repeated alternating stimuli.

Still, it was possible that CaM is permanently bound to the channel and participates in the gating machinery while only inhibiting the current when bound to Ca^{2+}. Although the available literature would not be compatible with this hypothesis (Schonherr et al. 2000; Ziechner et al. 2006)), we estimated the fraction of channels (WT or mutant) bound to CaM as a function of free Ca^{2+} concentration. We co-expressed Myc-tagged CaM and $K_V10.1$, extracted the proteins in different Ca^{2+} concentrations (see Methods), and pulled

down the complex through the Myc-tag of CaM. Under these conditions, we could consistently detect a fraction of channels bound to CaM already in 50 and 100 nM Ca^{2+}, which increased dramatically in 0.5 and 1 μM, compatible with previous reports, suggesting that, at basal Ca^{2+}, only a small and variable fraction of channels are bound to CaM both in the WT and in the mutants (Supp. 4 to Fig. 8). The fraction of channels bound to CaM at basal Ca^{2+} (in the range of 4% in 100 nM), even if only one CaM is needed per channel tetramer, is insufficient to explain the prominent and proportionally constant first component observed in the mutants.

In summary, our results strongly suggest that Ca^{2+}-CaM stabilizes O_1, possibly by driving the channel to deep closed states.

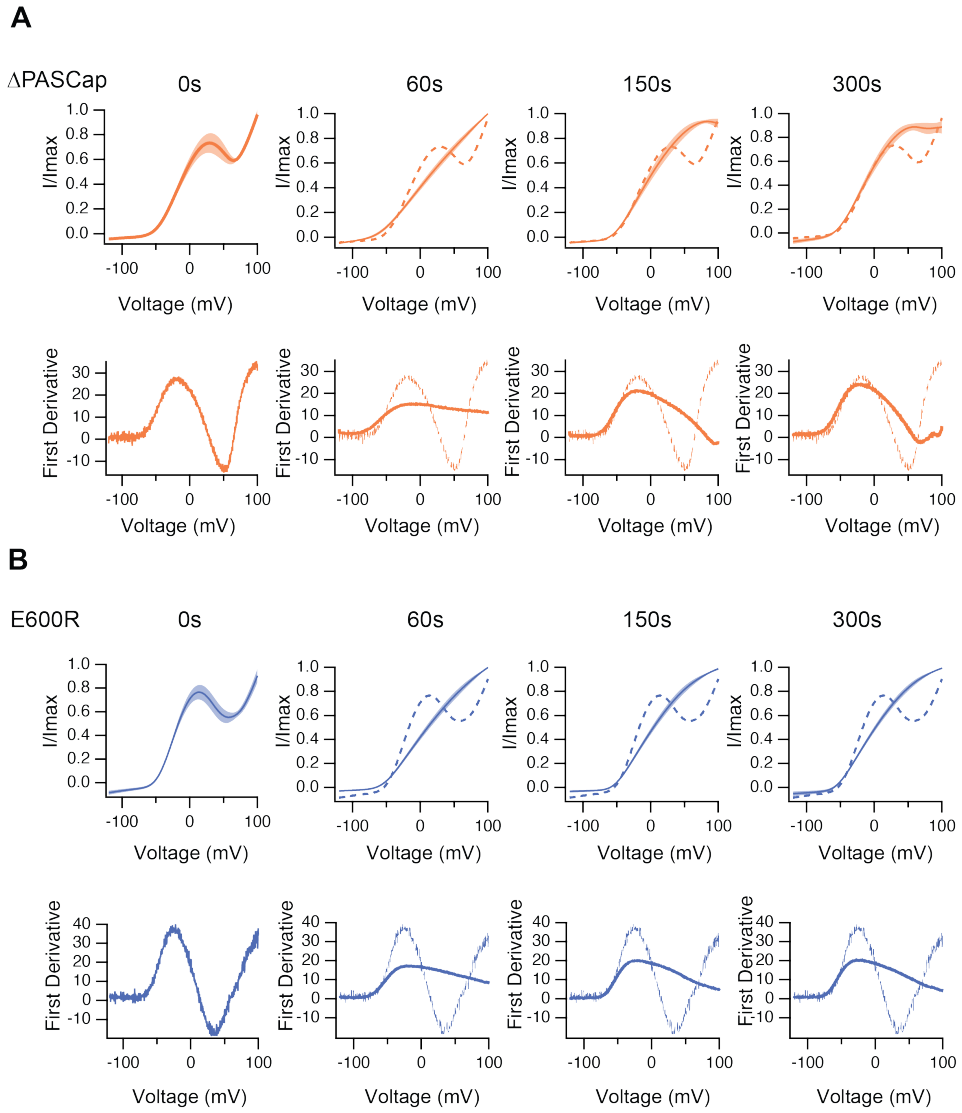

Supplement 2 to Figure 8. The upper traces show the average of normalized ramps at the indicated times for ΔPASCap (**A**) and E600R (**B**) after induction of Ca^{2+} rise. At 60, 150 and 300 s, the dashed line corresponds to the ramp at time 0. The shadowed area indicates SEM (N: ΔPASCap = 8, E600R = 10). The lower panels correspond to the first derivative of the current traces to illustrate the changes in slope.

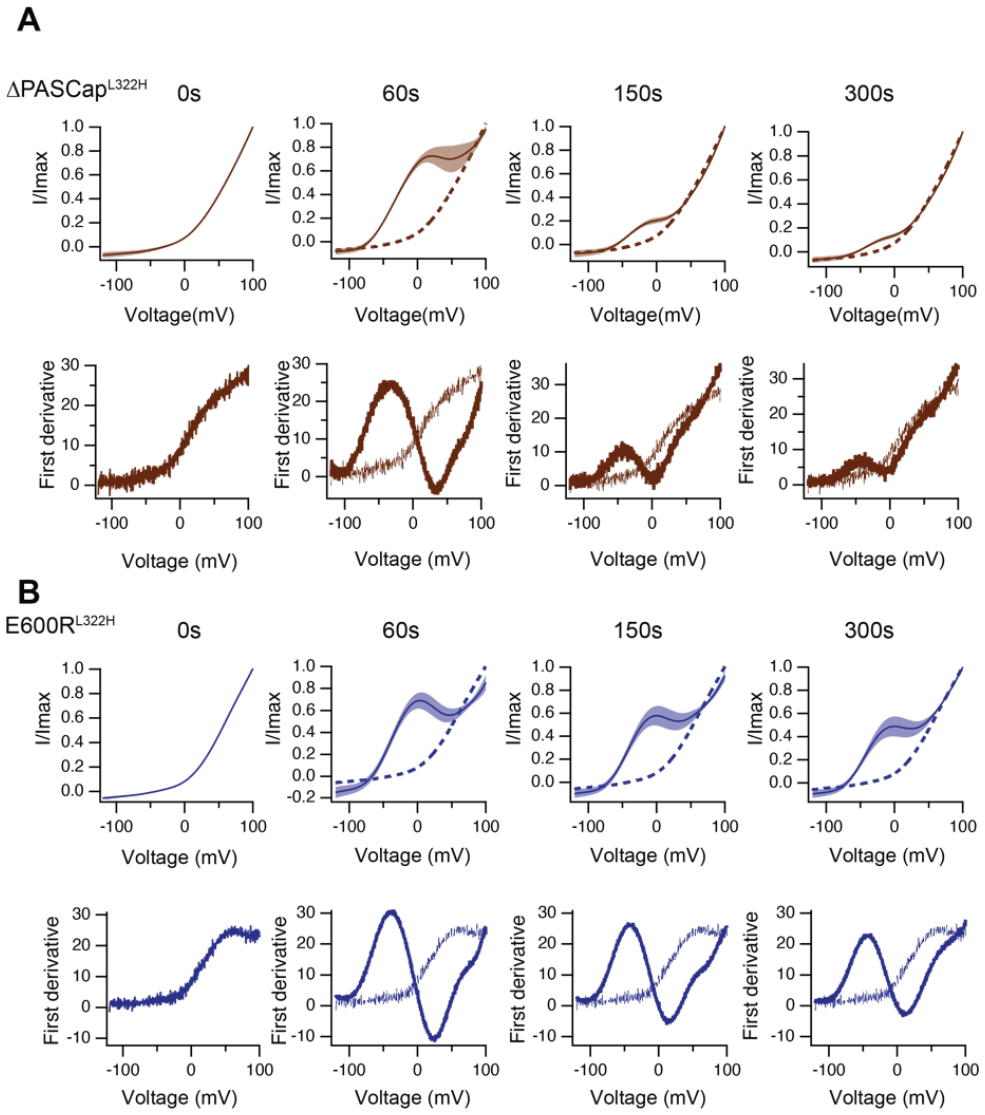

Supplement 3 to Figure 8. Like in Supplement 2, the upper traces show the average of normalized ramps for $\Delta PASCap^{L322H}$ (**A**) and $E600R^{L322H}$ (**B**) at the indicated times after induction of Ca^{2+} rise. At 60, 150 and 300 s, the dashed line corresponds to the ramp at time 0. The shadowed area indicates SEM (N: $\Delta PASCap^{L322H}$ = 5, $E600R^{L322H}$ = 11). The lower panels correspond to the first derivative of the current traces to illustrate the changes in slope.

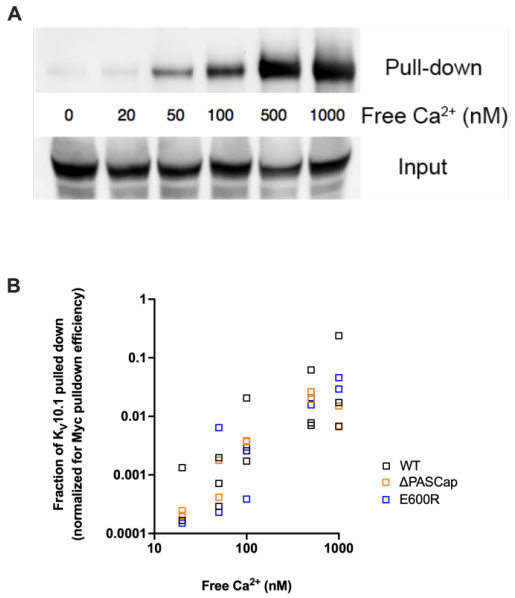

Supplement 4 to Figure 8. A. Ca^{2+}-dependent binding of CaM to $K_V10.1$. CaM was precipitated with anti-Myc antibody and the resulting pulled down fraction was immunoblotted using polyclonal anti- $K_V10.1$ antibody. **B** Quantification of all experiments reveals a strong dependence on Ca^{2+} concentration in WT and to a similar extent in mutant channels. The fraction of $K_V10.1$ pulled down increases by two orders of magnitude in high Ca^{2+}.

A two-layer Markov model recapitulates the kinetic features of ΔPASCap.

So far, our experimental results suggest that an additional open state exists in $K_V10.1$ mutants with a compromised intramolecular coupling. This hypothesis can explain the biphasic GV curves, the tail currents' complex shape (Fig. 1 and 2), the current increase following repeated brief hyperpolarizations (Fig. 4), and even the paradoxical current increase under rising intracellular Ca^{2+} concentrations (Fig. 8 and its supporting figures). However, in each case, there might be alternative explanations, such as two separate channel populations with different properties or voltage-dependent de-inactivation. The ultimate test for the hypothesis is the construction of a single model that consistently and quantitatively captures all these unusual characteristics.

It should be noted that the model structure presented here (Suppl. 1 to Fig. 9) is not the only one we found to be able to reproduce the data, but it is amongst the simplest that could (see Methods).

Given the large number of model parameters (42+absolute conductance), it might be surprising that all parameters can be constrained. However, the wide range of voltage protocols and the concurrent matching of depolarization and repolarization responses tightly constrains several rate ratios at different voltages and, thereby, ultimately all parameters. This said, the model never fitted all experiments at once very well. Consequently, a global fit proved extremely hard to achieve in an automated way, and we decided to explore the parameter space manually, based on the time constants and rate ratios we could discern from the experiments.

The model parameters are listed in Table S2. These parameters and the structure in Supplement 1 to Fig. 9 jointly define the model that produces all results in Fig. 9 and its supplementary figures for ΔPASCap.

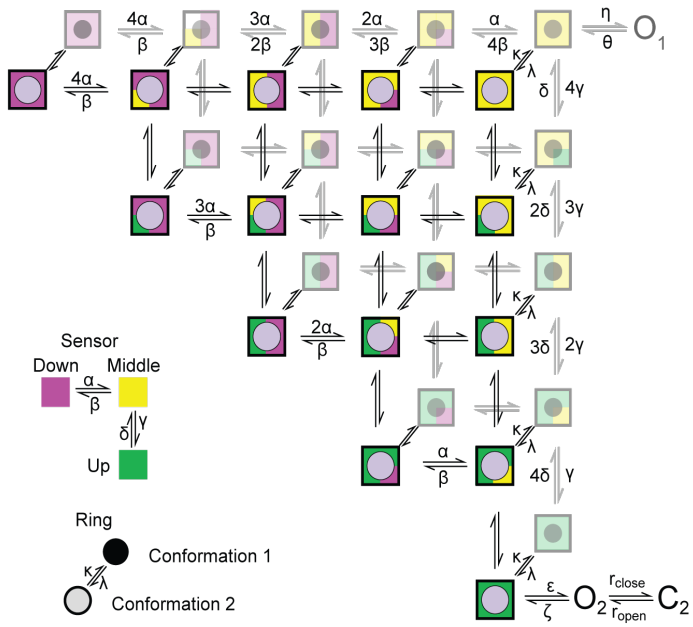

Supplement 1 to Figure 9. Cartoon depicting the state model proposed. A two-layer Markov-Model depicting possible conformations for the sensor and the ring. The sensor in each subunit can independently adopt one of three conformations (up, middle, and down) (Han et al., 2023). The up conformation represents the active conformation. The conformation of the ring changes across the two layers. The second conformation in the upper layer allows the channel to access "O_2" provided that all sensors are in the up conformation. Transitions within each layer is governed by (α, β, γ, δ), we proposed that the transitions are identical in the two layers. Transitions between the two levels are governed by the rate constants κ and λ

Modifications are only necessary to capture the effect of Ca^{2+}-CaM-binding and the properties of other channel variants. Suppose the binding influences the interaction between the intracellular modules that stabilize different configurations of the gating ring, e.g., BDC2, CNBHD, BDC1, and PASCap. In that case, the free energy of these states will change upon Ca^{2+}-CaM binding. Consequently, the free energy difference between the states, and thereby the apparent voltage sensitivity of the transitions, will change too. Hence, we represented the effect of different degrees of Ca^{2+}-CaM binding as different voltage shifts in λ, κ_L, γ, as indicated in Figure 9E.

	K_V10.1 ΔPASCap				K_V10.1 E600R				K_V11.1			
rate x	x_0 [s^{-1}]	A_x [s^{-1}]	V_{hx} [V]	K_x [V^{-1}]	x_0	A_x [s^{-1}]	V_{hx} [V]	K_x [V^{-1}]	x_0	A_x [s^{-1}]	V_{hx} [V]	K_x [V^{-1}]
α	8	192	0.09	-55	8	192	0.09	-55	0.5	99.5	0.09	-30
β	4	596	-0.13	80	4	596	-0.13	80	1.2	16.8	-0.1	80
γ	5	595	0.05	-30	5	595	0.05	-30	2.5	297.5	0.05	-30
δ	15	235	0.055	30	15	235	0.055	30	7.5	117.5	0.025	30
ε	200	0	—	—	200	0	—	—	200	0	—	—
ζ	660	0	—	—	1440	0	—	—	24000	0	—	—
η	80	320	0	-80	80	320	0	-80	80	320	0	-80
θ	16	44	0	-50	16	44	0	-50	16	44	0	-50
κ_R	0.125	69.875	-0.1	200	0.125	69.875	-0.1	200	0.65	119.35	-0.1	200
κ_L	0.125	499.875	0.09	-130	0.125	499.875	0.09	-130	0.65	499.35	0.09	-130
λ	0.1	999.9	-0.12	170	0.1	999.9	-0.12	170	0.1	999.9	-0.115	180
r_{open}	100	0	—	—	30	0	—	—	30	0	—	—
r_{close}	450	0	—	—	330	0	—	—	5970	0	—	—

Table S2: parameters describing the voltage dependence of the transitions between states in the Markov model of K_V10.1 ΔPASCap, K_V10.1 E600R, and K_V11.1 in conjunction with Eq. 6 and the structure in Supp. 1 to Fig. 9.

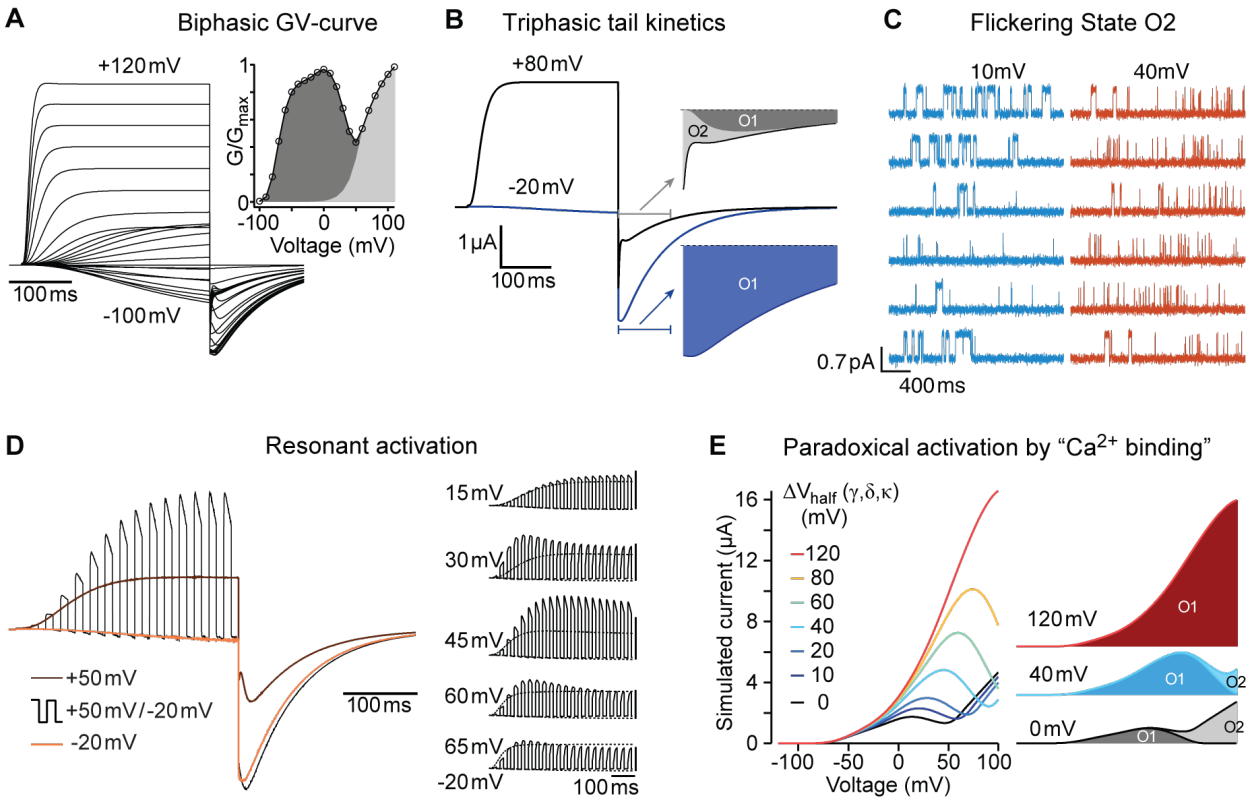

Figure 9. A single model can reproduce all experimental observations. A. In response to an I-V-protocol (Fig. 1A), the model displays biphasic activation, more clearly represented in the derived G-V curve (right, compare to Fig. 1B). The filled area indicates the contributions of the two open states. The tail-currents show a complex dependence on test-pulse voltage and time. **B**. Two traces from A, shown with longer repolarization. The first 100 ms of the tail currents are displayed on an extended timescale. Colored areas indicate the contributions of the two open states. After weak depolarization to -20 mV, the tail-current originates almost entirely from the mutant-specific open state O_1 (blue area). After strong depolarization, O_2 mediated currents initially dominate (light grey). For details, see Supplement 2 to Figure 9. **C.** The model predicts the differences in single channel behavior of ΔPASCap upon depolarization to +10 or +40 mV (Compare to Figure 5). **D**. In response to 10 ms pulses alternating between -20 and +50 mV, the model shows currents that exceed the currents obtained with constant pulses to +50 mV (compare Fig. 4 B). Relating the currents during the positive and negative pulses to the concurrent currents elicited by the two constant pulses (brown and orange), the ratio lies by about 1.6 for the period starting 200 ms after the pulse onset. This excess current depends sensitively on the duration and voltage of the two pulse components. The right series of simulations displays the results for 15 ms pulses to -20 mV, alternating with 15 ms pulses to voltages from 15 mV to 65 mV. The corresponding responses to the constant pulses are displayed with thin dotted lines. To facilitate perception of the excess current, the five groups of traces are scaled individually, so that the peak amplitude of the dotted response elicited by the stronger depolarizations is displayed at equal size throughout. The vertical scalebars correspond to the same absolute current. From top to bottom, the excess current ratios at 200 ms changes are 1.05, 1.38, 1.74, 1.46, and 1.16. **E**. The binding of Ca^{2+}-CaM is implemented through change in the activation energy, corresponding to a shift in the equilibrium voltage of the gating transitions. The decomposition of the current into the individual open states' contribution shows that for increasing voltage shifts – representing high $[Ca^{2+}]_i$ – the mutant-specific O_1 closes later into the ramp, until eventually all current is carried by O_1.

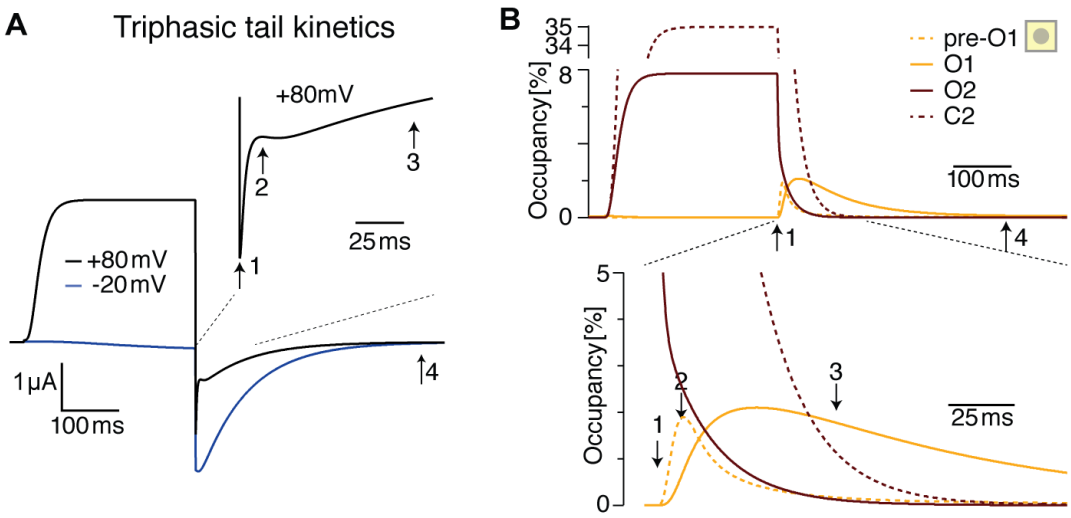

Supplement 2 to Figure 9. The triphasic tail currents result from transient re-population of O_1 during channel deactivation **A**. Simulated currents from Fig 9 B display simple, monophasic tail currents after weak depolarizations but triphasic tail current after +80 mV depolarization, similar to experimental results (see Fig. 1E). **B**. Occupancy of O_2, O_1 and its neighboring state as a function of time during a depolarization to +80 mV and repolarization to -100 mV. The three phases result from rapid initial vacation of O_2, followed by a slower process resulting from the delayed vacation of C_2 through O_2. This results in an increased occupancy of the neighboring state to O_1 (pre-O_1), which drives a transient increase in O_1 occupancy that is the basis for the transient tail current increase around time point 2. Slowly, deeper closed states are repopulated, and in the process, pre-O_1 and eventually O_1 fall empty from time point 3 to 4.

While the Markov model describes the time and voltage dependence of state occupancies, the experimental observable is current. From the model's occupancies, current was obtained by application of the GHK flux equation (equation 5) for both open states. While the single channel conductance of the two open states in the model is identical, the effective occupancy of O_2 and, thereby, its macroscopic conductance is drastically reduced by a flicker block, a rapid transition into C_2, and a slower return to O_2. To match experimental results, in particular the pre-pulse-dependent activation and tail current amplitudes, the flickering kinetics had to be adjusted to achieve a limiting occupancy ratio of 5.5 between C_2 and O_2, i.e. $r_{close}/r_{open=}$ 4.5. Typically, flicker-closures are thought to result from instabilities of the open state, unrelated to voltage sensor rearrangements. Here, r_{close} and r_{open} are constant and voltage-independent. The range of plausible absolute values for r_{close} and r_{open} is well constrained by experiments. If, following strong depolarizations, O_2 is populated faster than it is vacating into C_2, a transient overshoot appears shortly after depolarization onset. This is observed in E600R, but not ΔPASCap (Figure 1A and 1C). We found that the E600R observations can be mimicked with r_{open}=30, while mimicking ΔPASCap activation requires at least r_{open}=100. Further increases induce only small changes, visible in the triphasic tail current kinetics. In the limit of very fast flickering kinetics, the model becomes indistinguishable from a model without flickering in which O_2 microscopic conductance is reduced to 1/5.5.

To test the model, we focused on the most conspicuous kinetics features observed with ΔPASCap. The first feature was the tail kinetics. In contrast to the slow monophasic deactivation observed in response to *weak* depolarizing pulses (-20 mV), triphasic tail kinetics was detected in response to *strong* depolarizing pulses (+80 mV) (Fig. 1C). The model could replicate the slow deactivation after *weak* depolarizations, fast after *strong* depolarizations, and mixed kinetics on *moderate* stimuli (Fig. 9B; Supp. 2 to Fig. 9).

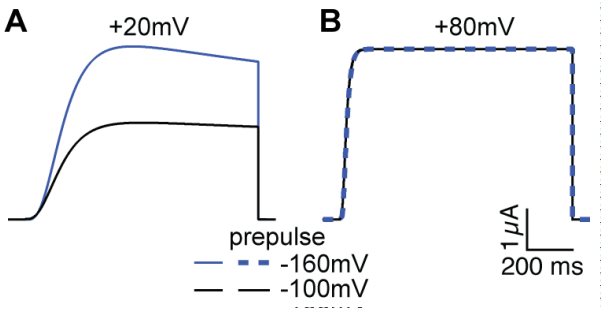

Supplement 3 to Figure 9. Current simulations for ΔPASCap upon depolarization to +20 and +80 mV after a conditioning pulse to -160 or -100 mV. The current at +20 mV is larger after -160 mV, while the current at +80 mV is unaffected by the conditioning pulse (see Fig. 6A)

The model also reproduces the effect of a hyperpolarizing prepulse on different test potentials. As described (Fig. 6), O_1 is preferentially accessed from deep closed states, which correspond to states towards the left in the lower layer in the model. It is plausible that a hyperpolarizing pre-pulse (-160 mV) drives the channel to occupy the deep closed states (lower layer), while a pre-pulse of -100 mV distributes the channel between both layers. We, therefore, adjusted the parameters accordingly (Table S2) and simulated the current trace (Supp. 3 to Fig. 9). We focused on a test pulse that represents *moderate* depolarizations (+20 mV), and compared it to a *strong* depolarizing pulse (+80 mV). Like in the experiment, the more strongly hyperpolarizing prepulse (-160 mV) potentiates the current at +20 mV, as compared to the prepulse to -100 mV (Supplement 3 to Fig. 9, A). This does not happen for the larger depolarization to +80 mV (Supp. 3 to Fig. 9, B).

The model also recapitulates the behavior of ΔPASCap during repeated short stimuli between -20 and +50 mV. The current amplitude driven by intermittent stimuli is larger than that driven by a sustained stimulus to the same potential. The model also reproduces the relative size and the kinetics of the tail current (Fig. 9C.; Supp. 4 to Fig. 9).

The effect of a rise in Ca^{2+} can be reproduced by shifting the voltage dependence of just two transitions (γ↔δ and κ). The rationale behind this that Ca^{2+}-CaM binding stabilizes the basal configuration of the ring and thereby shifts the activation energy for state transitions that are coupled to ring reconfigurations, i.e. the second VSD displacements (γ↔δ) and the ring gating itself (κ). Shifts in activation energy of voltage-dependent rates correspond to an extra term that can be expressed as voltage offset. When the voltage-dependence of these three rate constants is shifted by 10 to 120 mV, the occupancy of states in the "lower"

layer is increased and thereby the access to O_1 (Fig. 9D). The resulting simulated currents reproduce the experimental observations: a linear current response during ramps in high intracellular Ca^{2+}.

To describe the behavior of $K_V10.1$ WT, we only needed to remove the access to O_1 and shift the parameters of the rotation of the ring in the hyperpolarizing direction to reflect the more stable structure resulting from intact interactions among intracellular domains and between these and the core of the channel. The model recapitulated the change in kinetics depending on the pre-pulse potential.

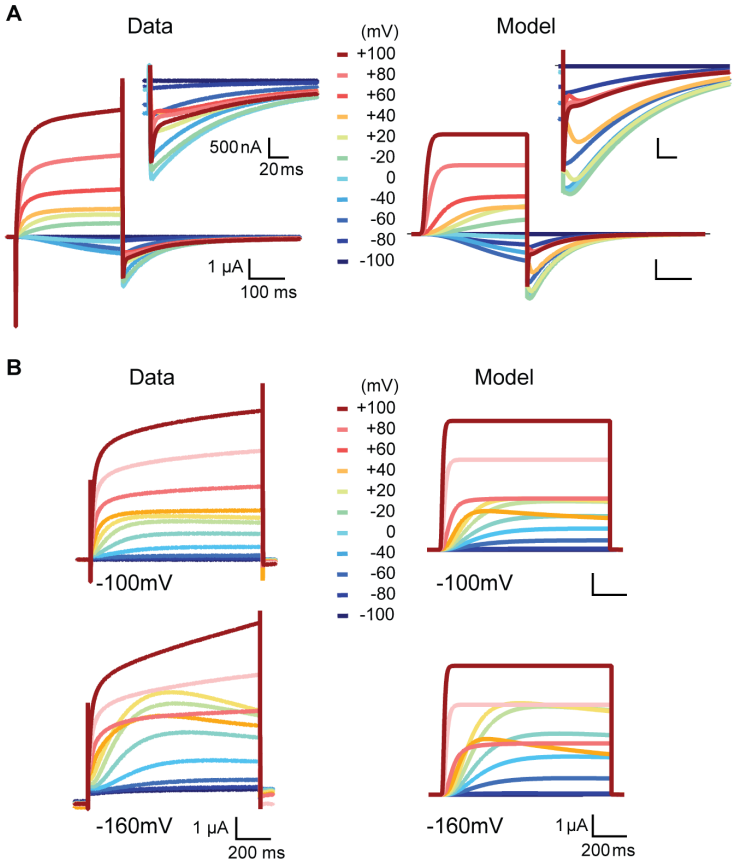

Supplement 4 to Figure 9. Side-by-side comparison of experimental data and model prediction during depolarizations between -100 and +100 mV in the presence of high (60 mM) (**A**) or low extracellular [K^+] (2.5 mM) (**B**). The model describes the features of the experimentally observed currents, except the sustained rising phase during strong depolarizations.

The model structure and the values of its parameters have been developed to reproduce the kinetic features of currents through $K_V10.1$ ΔPASCap channels. Can it provide insights into specific properties of other genotypes? A very palpable, E600R-specific feature is the transient current peak that occurs within about 30 ms after depolarizations above +70 mV (Fig 1A and 1C). It suggests that O_2, the open state underlying current at these voltages, is populated and vacated with very similar rates. In the model, such a transient

peak can indeed be reproduced if the rate constant from O_2 into C_2 (Supplement1 to Figure 9) is reduced from 100 s^{-1} for ΔPASCap to 30 s^{-1} for E600R (Supp. 5 to Figure 9). E600R also supports larger tail currents, relative to the test-pulse currents, indicating an even stronger bias away from O_2 into C_2. To replicate this, r_{close}/r_{open} was increased to 11 and the rate constant ζ, leading out of O_2 was adjusted to compensate for the lower O_2 occupancy. These few changes, all concerned with O_2 instability, underly the simulations in Supp. 5 A and B to Figure 9. The corresponding parameters are given in Table S2.

The tails observed in E600R show a shape reminiscent of that of $K_V11.1$, where slow deactivation is crucial for its physiological function. Our model can mimic $K_V11.1$ if the flicker block is biased further towards the closed state, and the transitions between closed states are slowed (Supp. 5 D and E to Figure 9 and Table S2),

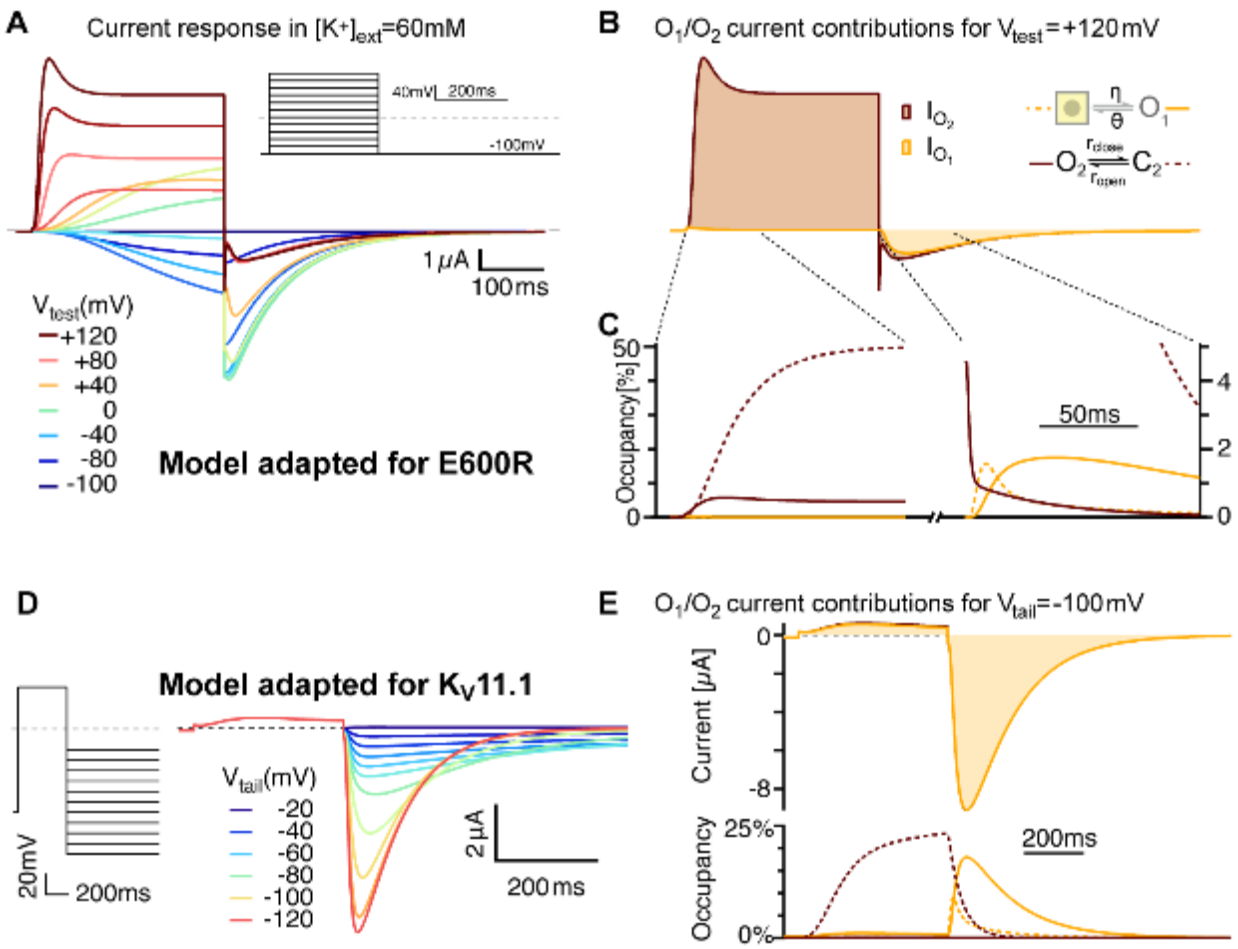

Supplement 5 to Figure 9: Model variants can account for features of related channels and mutated variants. **A** E600R gating features are consistent with slower flickering of a less populated O_2. After lowering the stability of O_2 (larger r_{close}/r_{open} and larger ζ/ε) and an overall slower flickering between O_2 and C_2 (Table S2), simulated currents show transient peaks during strong depolarizations and larger tails with more pronounced triphasic waveforms. Those features resemble the measurements with the E600R mutant (Fig 1A). **B** The relative currents of C_2 and O_2 differ even more than in the ΔPASCap model. The transient peak results from a delayed O_2-C_2 equilibration due to reduced flicker rates. Traces are shown in the same units as in A. **C** As close-up of the states' occupancies shows that the mechanism

of triphasic tail currents remains the same in the E600R model version (compare Supplement 2 to Figure 9). **D** The model recapitulates key features of Kv11.1 when the balance between O_2 and C_2 is further biased towards the closed state and with slowed transitions between closed states (see Table S2). The traces were generated for high extracellular $[K^+]$ (50 mM), to allow for comparison with experimental recordings in (Lörinczi et al. 2015).

Discussion

The wide diversity of electrical responses in cells relies greatly on subtle differences in the behavior of voltage-gated channels. Despite the many relevant advances in the knowledge of the structure of ion channels, the correlation between the structures and the functional determinants of channel behavior is incompletely understood. In this study, we have combined biophysical, biochemical, and mathematical approaches to understand the complex gating behavior of $K_V10.1$ potassium channels, which is the basis of a group of diseases with devastating consequences (e.g. (Toplak et al. 2022; Tian et al. 2023)).

In *KCNH* channels, intracellular domains contribute to gating by forming an intracellular ring that rotates in response to depolarizing stimuli (Mandala and MacKinnon 2022). We have studied a series of mutant channels where the integrity of the intracellular ring is compromised by either deletions or point mutations. In all the mutants, the G-V relationship shows a biphasic behavior with evident inward rectification at intermediate depolarizations and a complex deactivation with kinetics also dependent on the stimulus potential (Fig. 1). Our observations can be explained by the coexistence of two different open states, one of which corresponds to the open state observed in WT (O_2), while the other one (O_1) is made visible as a result of the modification of the intracellular gating ring. We hypothesize that O_1 corresponds in the WT to the "non-conducting state 2" identified in the closely related $K_V10.2$ channel by cryo-EM (Zhang et al. 2023), in which flipping of Y460 (Y464 in $K_V10.1$) renders a hydrophobic constriction wider than 8 Å, enough to allow K^+ flow, but still corresponds to a non-conducting state. The presence of an intact intracellular ring would preclude ionic flow in the WT, and its alteration would explain the permeability of this state in the mutants.

The coexistence of two independent channel populations with different gating properties could be an alternative explanation for the observed behavior. Still, it is very unlikely that two such populations would be expressed at the same ratio in all oocytes, given the variability of the system, and the behavior of each of the mutants was highly reproducible among oocytes obtained from different frogs and time points. Furthermore, activity in excised patches from oocytes expressing mutant channels was abolished in the presence of astemizole.

The atypical open state O_1 allows the study of intermediate steps between the two major gating events, VSD displacement and ring rotation. Upon intermediate depolarization, the channels would access the open states sequentially, while O_2 is predominant on strong depolarizing steps and O_1 upon mild stimuli. The analysis of the GV of the mutants using global parameters (Fig. 2) revealed that they all share the component responding to mild depolarizations (O_1) and only the second component (O_2) and (probably most importantly) the transition between components depends on the particular mutant studied. The larger the deletion in the intracellular ring is, the stronger the shift in the voltage dependence of the second component.

Importantly, this observation is also incompatible with two independent populations of channels. Since the two gating steps are sequential (Mandala and MacKinnon 2022), the displacement of the VSD remains the main factor governing the speed and voltage dependence of the activation. Thus, changes in the extracellular Mg^{2+} concentration, which are known to interfere with the movement of the VSD (Bannister et al. 2005; Silverman et al. 2004), cause a shift of the voltage dependence and activation speed that affects both gating components (Fig. 3), but not the transition between them.

The biphasic behavior arises from a different apparent conductance between the two open states, with larger open probability and, therefore, larger macroscopic amplitude for O_1. This results in a decrease in current amplitude as the channels leave O_1 and transition to O_2. Since the time required to access the two states is different, when short alternating stimuli are applied, each with a too short duration to allow entry into O_2, the longer open time of this state results in a larger current amplitude than when a single sustained stimulus is used (Fig. 4). The presence of a second state with larger or longer openings when the integrity of the ring is compromised could explain the larger current amplitudes observed in heteromeric $K_V11.1$ (HERG1a/1b) channels, which lack at least one PAS domain as a result of alternative splicing and are crucial for proper cardiac repolarization (Feng et al. 2021). Thus, the second open state could also have physiological relevance in naturally occurring channel complexes.

Access to O_1 is favored from deep deactivated states, which appear important in other aspects of $K_V10.1$ channel function (e.g., Cole-Moore shift). Our conclusion is based on the changes in amplitude observed with different pre-pulse potentials (that is, driving the population to deep closed states, Fig. 7A and B) and on the behavior of a mutant known to hinder access to such deactivated states (L322H), which, when combined with mutations revealing O_1, shows limited access to this state (Fig. 7C and D).

Ca^{2+}-CaM is an important modulator of $K_V10.1$ that reduces WT current amplitude in the presence of elevated Ca^{2+} levels. A paradoxical current increase had been described for some of the mutants used in this study (Lörinczi et al. 2016), and we speculated that the presence of O_1 could be the basis for this phenomenon. Indeed, the elevation of intracellular Ca^{2+} leads to a transient loss of the biphasic behavior and a larger current amplitude of the mutants compatible with a larger fraction of channels in O_1. Because access to O_1 occurs from deep closed states, this could be explained by an increased occupancy of such deactivated states in response to CaM binding. This appears to be the case since CaM induces a biphasic behavior in the mutant channels that show reduced access to deep closed states; thus, L322H mutants behave like the parental variants in the presence of Ca^{2+}-CaM. This implies a mechanistic explanation for the effect of Ca^{2+}-CaM on WT since favoring entry into deep closed states would result in a decrease in current amplitude in the absence of (a permeable) O_1.

Our initial hypothesis that CaM participates constitutively in the gating machinery of the channel, based on the loss of biphasic behavior when the C-terminal binding site for CaM was mutated (Fig. 8D), is unlikely to be correct because although there is a significant binding of CaM to the channel at basal intracellular Ca^{2+}, this fraction of channels, combined with the strong increase in bound CaM in the presence of high Ca^{2+} and the variable intracellular basal Ca^{2+} in oocytes would be insufficient to explain the qualitatively consistent behavior of the current of the different mutants. We speculate that the effects of the mutations in CaM binding sites are more related to their location in the protein than to their ability to bind CaM.

In summary, the gating of $K_V10.1$ (and similar channels) consists of a sequence of events that affect the voltage sensing domain, which moves in two sequential steps (Schonherr et al. 1999) and whose movement is transferred to the pore domain through intramolecular interactions (Bassetto et al. 2023). The voltage sensor maintains the gate closed (Mandala and MacKinnon 2022), and its displacement has a permissive effect on the gate opening. Once this restrictive factor is removed, a second step occurs, most likely corresponding to a rotation of the intracellular ring that finally allows the gate to relax to the open state (Patlak 1999). This final step is the only one directly observed in WT channels.

We proposed the existence of a second open state in $K_V10.1$ with an altered eag domain, because that could readily explain otherwise puzzling observations in macroscopic recordings. Our single channel recordings provided definitive evidence for channel openings with two different kinetic characteristics. Finally, w constructed a Markov model of $K_V10.1$ mutants' gating that replicates all key experimental observations (Fig. 9 and its supplements). This model performance required two modifications to previously established K_V10 models: 1. introduction of an additional open state with a larger macroscopic current and 2. an additional gating step orthogonal to the previously described state plane. This added a second layer of states. Steps within each layer correspond most likely to two sequential displacements of the four VSD. Steps between the layers are interpreted as reconfiguration of the intracellular ring. The new state O_1 is already accessible when the first displacement of all four VSD is completed but the ring has not changed, while entry into O_2 requires complete VSD displacements and ring reconfiguration. The rapidly flickering open state of O_2 observed in the single channel recordings, is realized in the model by rapid, voltage-independent gating in-and-out of a neighboring closed state (C_2). This flicker block might also offer an explanation for a feature of the mutant channels, that is not explained in the current model version: the continued increase in current amplitude, hundreds of milliseconds into a strong depolarization (Supp. 4 to Fig. 9). If the relative stability of O_2 and C_2 continued to change throughout depolarization, such a current creep-up could be reproduced. However, this would require either the introduction of further layers of $O_n \leftrightarrow C_n$ states, or a non-Markovian modification of the model's time evolution.

To which degree does the model reflect the topology and gating transitions of $K_V10.1$ mutants? By construction, the presented model has one of the simplest structures that can replicate all key findings. Specifically, a model with less than three different gating steps, (two VSD, one ring), without flicker block, or with O_1 and O_2 in close proximity would fail to replicate at least one of the key findings. With respect to these fundamental properties, the model's structure should mirror the fundamental properties of $K_V10.1$ gating. The finer details of the model structure are less certain; we were able to vary them without large improvements in performance, but also without clear losses. This includes the feature that trans-layer connections exist for each state except the open states and the flicker block, and the feature of complete equivalence of the VSD transitions within lower and upper layer. Those features were made as choices for simplicity and symmetry. One price for the simple structure is the relative complex voltage dependence of the rates. The functional form of the rates' voltage dependence is an often-underappreciated way to shift model complexity from the state diagram to the rate functions. Following Arrhenius or Eyring formalisms, transition rates are expected have the form $c_0 \cdot \exp(\Delta V/k)$ and range from zero to infinity without saturation or a non-zero minimal rate. If, however, a transition between two states ($\leftrightarrow S_1 \leftrightarrow S_2 \leftrightarrow$) is used as a shorthand for an underlying linear three-state system ($\leftrightarrow S_1 \leftrightarrow S_2 \leftrightarrow S_3 \leftrightarrow$), in which only the transition $S_1 \leftrightarrow S_2$ is voltage-dependent, while $S_2 \leftrightarrow S_3$ features constant forward and backward rates, then the current activation kinetics in the two-state shorthand will saturate even for infinitely high voltages. Similarly, a non-zero basal rate x_0 can be caused by an alternate "leakage" route from the first state S_1 to the open state O that occurs at a very low, voltage-independent rate. In the light of such considerations, the sigmoidal voltage dependences of the model's rates point to a much more complicated underlying structure.

A large majority of ion channel models in use today uses voltage dependent rates with functional forms that are more complex than a simple exponential. Although in general, we prefer the use of the simple forms (e.g. (Yang et al., 2016)), in the present case, we decided to keep the model structure as simple as possible and use a more complex voltage dependence of the rates, to avoid adding even more states. As a consequence, some voltage dependencies can raise questions about how the model corresponds mechanistically to underlying gating steps. In particular rate κ, governing the transition from the newly introduced upper floor to the ground floor, is described by a sum of two voltage dependencies of opposite sign. The necessity for such a complex voltage dependence clearly signals unresolved structural details. What's more, the κ/λ transition could reasonably be expected to be voltage independent because we related it to ring reconfiguration, a process that should occur as a consequence of a prior VSD transition. We have made some attempts to treat this transition as voltage independent but state-specific with upper-layer bias for states on the right and lower-layer bias for states on the left. This is in principle possible, as can already be gleaned from the similar voltage ranges of the left-right transition (α/β) and the κ_L/λ transition. However, this approach leads to a much larger number of free, less well constrained kinetic parameters and drastically

complicated the parameter search. The model version presented here is therefore a low-complexity compromise that showcases the explanatory power of a second open state and an additional gating step.In summary, this study presents a more complete description of the gating mechanism of $K_V10.1$ channel, which, importantly, can be extended to other members of the *KCNH* family. In response to depolarization, the movement of the voltage sensor would have a permissive role in the opening of the gate. The rotation of the intracellular ring would be the effective unlocking mechanism allowing permeation. This has profound implications pertaining to the possibilities of fine-tuning gating since the intracellular ring is more susceptible to posttranslational modifications and protein-protein interactions than the transmembrane domains. Our current knowledge of the physiology and pathophysiology of $K_V10.1$ indicates that the channel is relevant for the regulation of excitability acting at potentials close to the resting rather than during active electrical signaling. Therefore, sustained modulation of gating, possible through modification of the intracellular ring, would be crucial for channel function. Since they allow dissection of the ring-dependent effect, our mutants will allow for a direct study of such modulation mechanisms.

Materials and Methods

Constructs

Mutants were generated using K_V10.1 (hEAG1) cloned in pSGEM (M. Hollmann, Bochum University) as a template (Jenke et al. 2003). The deletion mutants, Δ2-10 and ΔPASCap, were generated using In-Fusion HD Cloning kit (Clontech (TaKaRA)) following the supplier's instructions. For each construct, we designed two primers, each of them with two regions: a 3' region that anneals to the template immediately up- or downstream of the sequence to be deleted and a 5' that does not bind to the template but overlaps with the second primer (Table S3). The subsequent PCR amplification will then omit the sequence between the hybridization sites for the primers.

To generate the point mutations (ΔPASCap^{L322H}, ΔPASCap^{BDN}, ΔPASCap^{BDC2}, E600R^{L322H}, E600R^{BDN}, E600R^{BDC2}), site-directed mutagenesis was performed using Quick Change II XL kit (Agilent Technologies) using the primers listed in Table S3. E600R.pLeics71 and Δeag.pLeics71 were a gift from Dr. John Mitcheson, University of Leicester.

The expression construct for 5-myc-calmodulin was obtained by restriction cloning of CALM1 from pKK233-hCaM, which was a gift from Emanuel Strehler (Addgene plasmid # 47598) (Rhyner et al. 1992) into a pSGEM construct with five consecutive repeats of the myc tag (Lörinczi et al. 2015)) using NcoI and HindIII (New England Biolabs).

All plasmids were linearized with NheI, and cRNA was synthesized using mMESSAGE mMACHINE T7 Transcription kit (Invitrogen Ambion).

Deletion/Mutation	Template (s)	Primers
Δ2-10	pSGEM.Kv10.1 pSGEM Kv10.1 L341Split	F attcgatatcaagcttatggtggcccctcaaaacacgtttct R cggtatcgataagcttcagctggctccaaaaatgtctctct
ΔPASCap 2-25	pSGEM Kv10.1	F gctgccgccaccatg aatgatactaattttgtgttggggaa R catggtggcggcagctcg
ΔCNBHD 525-697	psGEM Kv10.1.	F tccagaggcattgac aatgaggcccccctgatcttgc R gtcaatgcctctggacatggaccaa
L322H	pSGEM Kv10.1 ΔPASCap pSGEM Kv10.1 E600R	F gatgagggcatcagcagccatttcagctctctaaaagttgt R acaacttttagagagctgaaatggctgctgatgccctcatc
N-terminal CaM binding site (BDN) F151NL154N	pSGEM Kv10.1 Δ2-10 pSGEM Kv10.1 ΔPASCap	F151N ctcttgtcagccgagcattcttcccccagcctttac L154N tgcttgtcagtgctcttgtattccgagcattcttcccccag
C-terminal CaM binding site (BDC2) F714SF717S	pSGEM Kv10.1 Δ2-10 pSGEM Kv10.1 ΔPASCap	F714S gtcggaatctctggctgaggcgccggacag F717S ctgctgtcggcttctctggctgaggcgccgg

Table S3. Primers used for infusion cloning or site-directed mutagenesis. The sequences are listed 5'-3'. For mutagenesis primers, only the sense sequences are given. The reverse primers corresponded to the reverse-complement sequence.

Two-Electrode Voltage-Clamp Recordings

Oocyte preparation and injection were performed as described (Stühmer 1992). The amount of cRNA injected depended on the current amplitude obtained with each construct: 0.075 - 0.5 ng/oocyte (WT and point mutation), 0.075-5 ng/oocyte (deletion mutants), and 8-10 ng/oocyte (split channels). Oocytes were maintained at 18°C in ND96 buffer (in mM: 96 NaCl, 2 KCl, 1.8 $CaCl_2$, 1 $MgCl_2$, 5 HEPES, 2.5 Na-pyruvate, 0.5 Theophylline, pH 7.55). Tetracycline (USB) (50µg/ml), Amikacin (Enzo) (100µg/ml), and Ciprofloxacin (Enzo) (100µg/ml) were added as recommended in (O'Connell et al. 2011).

Two-electrode voltage-clamp (TEVC) recordings were performed 1-5 days after oocyte injection. The intracellular electrodes had a resistance of 0.4-1.5 MΩ when filled with 2 M KCl. Normal Frog Ringer solution (NFR): (in mM: 115 NaCl, 2.5 KCl, 10 HEPES, 1.8 $CaCl_2$, pH 7.2), was used as external solution. Higher K^+ concentration (mM: 60 KCl, 57.5 NaCl, 10 HEPES, 1.8 $CaCl_2$, pH 7.4), was used instead to examine tail currents. Cl^--free NFR (in mM: 115 Na-methanesulfonate, 2.5 KOH, 10 HEPES, 1.8 $Ca(OH)_2$, pH 7.2), was used to limit current contamination with Cl^- current; in this case, agar bridges (2% agar in 3 M NaCl) were used for the reference electrodes. To raise the intracellular Ca^{2+} concentration (Lörinczi et al. 2016), 5 µM ionomycin (Abcam) and 5 µM Thapsigargin (Abcam) were added to the bath. Ionomycin and Thapsigargin 5 mM stocks were prepared using DMSO and diluted in the recording medium (Cl^--free NFR) immediately before recording. The final concentration of DMSO was thus 0.1%.

Data acquisition was performed using a TurboTEC 10-CD amplifier (npi Electronics) and the ITC-16 interface of an EPC9 patch-clamp amplifier (HEKA Elektronik). The current was filtered at 1.3 KHz and sampled at 10 KHz. Patchmaster software (HEKA Elektronik) was used to design and apply the stimulus protocols applied. Because of the profound effects of hyperpolarization on channel kinetics, leak subtraction was avoided except when explicitly indicated. Linear leak was subtracted offline assuming a reversal potential of 0 mV. Fitmaster (HEKA Elektronik) and IgorPro (WaveMetrics) were then used to analyze the recordings.

Most conductance-voltage plots were obtained for recordings with $[K^+]_{ext}$ =60 mM. In this condition, tail currents are large and allow precise estimation of the reversal potential V_{eq}. Under this condition, the difference between intra- and extracellular potassium concentration is small and the Goldman-Hodgkin-

Katz flux equation predicts a nearly linear relation. In these cases, overall conductance was calculated from the end-pulse current after measuring the reversal potential (V_{eq}) using:

$$G = I / (V_m - V_{eq}) \qquad \text{Eq.2}$$

where I is the current amplitude and V_m the stimulus. Reversal potential was calculated using the end pulse current for mutant channels activating below the equilibrium potential for potassium, or instantaneous IV using tail currents for channels opening at more depolarized potentials. Conductance was then normalized to the maximum value and plotted against voltage stimulus. For WT recordings (Fig. 1B), a sigmoidal response was then fitted with a Boltzmann equation:

$$f(V) = \left(1 + \exp\left((V_h - V_m)/K\right)\right)^{-1} \qquad \text{Eq.3}$$

With V_h being the voltage for half-maximal activation, K the slope factor and V_m the membrane potential as above.

The biphasic response we observed in the mutants was described with two sigmoidal components and a weight W to represent the transition between the two components. The equation used was as follows:

$$f(V) = A_o + \left(1 - \mathrm{W}(V)\right) \cdot \mathrm{A}_1 \cdot \left(1 + e^{(V_{h1} - V_m)/K_1}\right)^{-1} + \mathrm{W}(V) \cdot \mathrm{A}_2 \cdot \left(1 + e^{(V_{h2} - V_m)/K_2}\right)^{-1}$$

$$\mathrm{W}(V) = \left(1 + e^{(V_{h3} - V_m)/K_3}\right)^{-1} \qquad \text{Eq.4}$$

If the currents were recorded in $[K^+]_{ext}$=2.5 mM, the driving force for currents becomes considerably non-linear (Kotler et al. 2022) and we estimated the conductance based on the full Goldman-Hodgkin-Katz flux equation for a current surface density Φ.

$\Phi = P \cdot P^{open} \cdot zF \cdot \frac{V_m}{V_T}\left(\frac{[K^+]_{in} - [K^+]_{out} \cdot e^{-V_m/V_T}}{1 - e^{-V_m/V_T}}\right)$, where $V_T = \frac{RT}{zF}$,with the gas constant *R,* the Faraday constant *F*, the absolute temperature *T*, the potassium channel open probability P^{open} , and the maximum permeability *P.* The ion's valence *z* equals 1. Because we only work with normalized conductances, the following relation can be used to determine the voltage-dependent conductance:

$$G(V) \propto I \cdot \left(\frac{1 - e^{-V_m/V_T}}{[K^+]_{in} - [K^+]_{out} e^{-V_m/V_T}}\right) \cdot \frac{V_T}{zFV_m}$$

Eq.5

Single-channel recording and analysis.

The vitelline membrane of oocytes expressing ΔPASCap cRNA, as described for two-electrode experiments, was mechanically removed after osmotic shock (Stühmer 1992) to expose the plasma membrane. Patch pipettes were pulled from thick-wall (0.5 mm) borosilicate capillaries to obtain a resistance of 7-12 MΩ when filled with the intracellular solution, which contained (mM) 100 KCl, 10 EGTA, 10 HEPES pH 7.2 (KOH). Recordings on outside-out patches were acquired using an EPC10 Plus amplifier and PatchMaster software (HEKA Elektronik). Currents were digitized at 10 kHz and filtered at 2 kHz. Analysis was performed using FitMaster. For presentation, the traces were digitally filtered at 100 Hz.

Pull-down

Xenopus laevis oocytes were co-injected with RNA coding for 5xmyc-calmodulin (10 ng) and $K_V10.1$ (0.5 ng). Oocytes were lysed 72 h after injection through mechanical disruption in lysis buffer and incubation for 30 min on ice. The lysis buffer (1% Triton X-100, 150 mM NaCl, 50 mM HEPES pH 7.4, cOmplete EDTA-free protease inhibitor cocktail (Roche)) contained different free Ca^{2+} concentrations (0, 20, 50, 100, 500, and 1000 nM). To obtain accurate Ca^{2+} concentrations, EGTA was titrated with $CaCal_2$, to prepare 100 mM CaEGTA stock solution as described in (Tsien and Pozzan 1989). CaEGTA and EGTA were then added to the lysis buffer, adjusting EGTA/CaEGTA to control the concentration of free Ca^{2+} taking into account pH, ionic strength and temperature of solution using MaxChelator (Bers et al. 2010). As controls, non-injected oocytes, and oocytes injected with only $K_V10.1$ or 5xmyc-calmodulin were lysed in a Ca^{2+} free buffer.

The lysate was then centrifuged (20,000 x*g*) at 4 °C for 3 min to remove debris. 10% of the supernatant was set aside to load on the gel as input control. The lysate was pre-cleared using protein G magnetic beads (New England Biolabs). The cleared supernatant was then incubated with 3 µg anti-myc antibody (SIGMA M4439 monoclonal anti c-myc or Abcam ab206486 rat mAb to myc tag (9E10)) for 1.5h at 4 °C. Protein G magnetic beads were then added and incubated for 1.5h at 4 °C in rotation. After magnetic retrieval, the beads were washed three times using 0.1% Triton X-100, 300 mM NaCl, 50 mM HEPES pH 7.4, cOmplete (EDTA-free protease inhibitor cocktail), EGTA and CaEGTA to obtain the corresponding Ca^{2+}-free concentrations (see above). Electrophoresis and immunoblotting conditions were as previously described (Lörinczi et al. 2015) using an anti-Myc (Sigma, 1:1000) or an anti-$K_V10.1$ antibody (Chen et al. 2011) overnight.

Markov-model construction

The standard model for $K_V10.1$ gating comprises two gating steps for each of the four subunits' voltage sensors. The first step unfolds in the hyperpolarized voltage range and forms the basis of the Cole-Moore shift, characteristic of $K_V10.1$ channel gating. The second, faster step readies the channel for opening, and once it is performed in all subunits, a conducting state can be reached (see also (Mandala and MacKinnon, 2022)). While this model captures the key features of WT activation, we had to extend it to account for the features of mutant gating. Throughout the model development and tuning, we focused on the experiments performed with the ΔPASCap mutant. However, a limited number of tests with other parameters showed that experimental findings with E600R and even with $K_V11.1$ can also be matched (Supp.5 to Fig.9).
In a first step, we attempted a minimal model extension by attaching an additional open state to some closed state of the standard model. None of the resulting models, for any choice of attachment site and rate voltage dependence, could replicate the multi-phasic tail currents, the pre-pulse dependent activation, and the delayed opening. We came to this conclusion in two steps. First, we could exclude many possible attachment sites because the attachment site must be sufficiently far away from the conventional open state. Otherwise, the transition from "O_1 preferred" to "O_2 preferred" via a few closed intermediate states is very gradual and never produces the biphasic GV curves. Second, we found that the first gating transition in the standard model (along α, left to right) can either produce a sigmoidal current onset or bias the model for occupancy of state O_1 over O_2, but not both. Waveforms such as the dark orange trace in Figure 6 A, in response to a -160 mV pre-pulse and a 20 mV test pulse require both a bias towards O_1 and a sigmoidal onset. We found that this can only be accounted for by introducing a third gating step orthogonal to the two transitions in the standard model.

Without *a priori* information about the new states introduced in this way, we decided to simply add a copy of the standard model as an additional layer, an "upper floor". Crossing from the ground floor to the upper floor was made possible for any state. From a structural view, this newly added transition might be related to a reconfiguration of the gating ring. Considerations as given above led us to attach the mutant-specific O_1 to the basal level and the conventional O_2 to the upper level. The experimental data indicated that O_1 had to be accessible to states “on the right of the ground floor”, that is, accessible from deep closed states. Along the same lines, O_1 could not be located “too far toward the bottom” of the scheme, because it is an open state. Eventually, we decided to attach O_1 only to the state that corresponds to the completion of the first gating step with no further transitions (neither the second voltage-sensor transition nor the gating ring transition) in all four voltage sensors. In contrast, to enter O_2, all subunits must complete both voltage sensor transitions and the collective gating ring transition. This model’s structure is displayed in Supp. 1 to Fig.9.

We also tested models in which the upper floor was only accessible from a subset of states and models with O_1 attached to more than a single closed state or even multiple O_1 states with varying conductance. While those more complex models offered a gradual improvement matching experimental traces, they showed no striking advantages over the more symmetric and parsimonious model presented here. Furthermore, we have extensively tested variants with a broken symmetry in the gating kinetics. In these models, the conventional gating steps (rates α, β, γ, δ) differed between the ground floor and the newly introduced top floor states, e.g., by the introduction of factors to the α, β, γ, δ values. Under these conditions, a local balance was achieved by corresponding inverse factors to the local κ and λ. Again, the gradual improvements that could be achieved did not seem to justify the introduction of the additional parameters.

Voltage dependence of rates

The simplest model structure that allowed us to reproduce the key observations (Supp. 1 to Fig.9) was implemented in Igor Pro as a system of coupled differential equations that govern the mean-field occupancies of the 33 states. To simulate the stochastic gating of a single channel, the Gillespie Algorithm was implemented (Gillespie 1976). For the voltage-dependent transition rates, we chose a sigmoidal functional form (Eq.6).

$$x = \mathrm{x}_0 + \frac{\mathrm{A}_x}{1+\exp\left(\left(V_\mathrm{m}-\mathrm{V}_x^\mathrm{h}\right)\cdot \mathrm{k}_x\right)} \qquad \text{Eq. 6}$$

where x stands for one of the rates α, β, γ, δ, that govern transitions in the first and second dimension of the model, which we attribute to two sequential steps of voltage sensor displacement. The rates η and θ of opening and closing of the mutant-specific open state O_1 also follow this functional form, as does the rate λ, governing the return from the upper layer. The rate κ of entering the upper layer is the sum of two components, $\kappa_{all} = \kappa_l + \kappa_r$, which again follow the same functional form. The rates leading towards and away from the second open state O_2, ε, ζ, r_{open} and r_{close} are constants.

Acknowledgements.

We thank the expert technical assistance of Kerstin Dümke. RA was supported by an IMPRS Neurosciences scholarship. This work was supported by Deutsche Forschungsgemeinschaft (DFG, German Research Foundation) Project-ID 436260547, in relation to NeuroNex (NSF 2015276) (to AN)

Data availability

The authors declare that the data supporting the findings of this study are available within the paper and its supplementary information files.

REFERENCES

Babu YS, Sack JS, Greenhough TJ, Bugg CE, Means AR, Cook WJ (1985) Three-dimensional structure of calmodulin. *Nature* 315:37-40. doi:10.1038/315037a0

Bannister JP, Chanda B, Bezanilla F, Papazian DM (2005) Optical detection of rate-determining ion-modulated conformational changes of the ether-a-go-go K+ channel voltage sensor. *Proc Natl Acad Sci USA* 102:18718-18723

Barros F, de la Pena P, Dominguez P, Sierra LM, Pardo LA (2020) The EAG Voltage-Dependent K(+) Channel Subfamily: Similarities and Differences in Structural Organization and Gating. *Front Pharmacol* 11:411. doi:10.3389/fphar.2020.00411

Bassetto CAZ, Jr., Costa F, Guardiani C, Bezanilla F, Giacomello A (2023) Noncanonical electromechanical coupling paths in cardiac hERG potassium channel. *Nat Commun* 14:1110. doi:10.1038/s41467-023-36730-7

Bauer CK, Schwarz JR (2018) Ether-à-go-go K+ channels: effective modulators of neuronal excitability. *The Journal of Physiology* 596:769-783. doi:10.1113/JP275477

Bers DM, Patton CW, Nuccitelli R (2010) A Practical Guide to the Preparation of Ca2+ a Buffers. *Method Cell Biol* 99:1-26. doi:10.1016/S0091-679x(10)99001-8

Busa WB, Nuccitelli R (1985) An elevated free cytosolic Ca2+ wave follows fertilization in eggs of the frog, Xenopus laevis. *J Cell Biol* 100:1325-1329. doi:10.1083/jcb.100.4.1325

Chen Y, Sánchez A, Rubio ME, Kohl T, Pardo LA, Stühmer W (2011) Functional Kv10.1 Channels Localize to the Inner Nuclear Membrane. *PLoS ONE* 6:e19257. doi:10.1371/journal.pone.0019257

Codding SJ, Johnson AA, Trudeau MC (2020) Gating and regulation of KCNH (ERG, EAG, and ELK) channels by intracellular domains. *Channels (Austin)* 14:294-309. doi:10.1080/19336950.2020.1816107

Codding SJ, Trudeau MC (2019) The hERG potassium channel intrinsic ligand regulates N- and C-terminal interactions and channel closure. *J Gen Physiol* 151:478-488. doi:10.1085/jgp.201812129

Cole KS, Moore JW (1960) Potassium ion current in the squid giant axon: dynamic characteristic. *Biophys J* 1:1-14. doi:10.1016/s0006-3495(60)86871-3

Dai, G., James, Z.M., and Zagotta, W.N. (2018). Dynamic rearrangement of the intrinsic ligand regulates KCNH potassium channels. *J Gen Physiol 150, 625-635. 10.1085/jgp.201711989.*

Dai G, Zagotta WN (2017) Molecular mechanism of voltage-dependent potentiation of KCNH potassium channels. *eLife* 6:e26355. doi:10.7554/eLife.26355

de la Pena P, Dominguez P, Barros F (2018) Gating mechanism of Kv11.1 (hERG) K(+) channels without covalent connection between voltage sensor and pore domains. *Pflugers Arch* 470:517-536. doi:10.1007/s00424-017-2093-9

Feng L, Zhang J, Lee C, Kim G, Liu F, Petersen AJ, Lim E, Anderson CL, Orland KM, Robertson GA, Eckhardt LL, January CT, Kamp TJ (2021) Long QT Syndrome KCNH2 Variant Induces hERG1a/1b Subunit Imbalance in Patient-Specific Induced Pluripotent Stem Cell-Derived Cardiomyocytes. *Circ Arrhythm Electrophysiol* 14:e009343. doi:10.1161/CIRCEP.120.009343

Gianulis, E.C., Liu, Q., and Trudeau, M.C. (2013). Direct interaction of eag domains and cyclic nucleotide-binding homology domains regulate deactivation gating in hERG channels. *J Gen Physiol* 142, 351-366. 10.1085/jgp.201310995.

Gillespie DT (1976) A general method for numerically simulating the stochastic time evolution of coupled chemical reactions. *J Comp Phys* 22:403-434. doi:10.1016/0021-9991(76)90041-3

Gonçalves JT, Stühmer W (2010) Calmodulin Interaction with hEAG1 Visualized by FRET Microscopy. *PLoS ONE* 5:e10873. doi:10.1371/journal.pone.0010873

Haitin Y, Carlson AE, Zagotta WN (2013) The structural mechanism of KCNH-channel regulation by the eag domain. *Nature* 501:444-448. doi:10.1038/nature12487

Harley CA, Bernardo-Seisdedos G, Stevens-Sostre WA, Jones DK, Azevedo MM, Sampaio P, Lorga-Gomes M, Trudeau MC, Millet O, Robertson GA, Morais-Cabral JH (2021) Conformation-sensitive antibody reveals an altered cytosolic PAS/CNBh assembly during hERG channel gating. *Proc Natl Acad Sci USA* 118. doi:10.1073/pnas.2108796118

Hoshi T, Armstrong CM (2015) The Cole-Moore Effect: Still Unexplained? *Biophys J* 109:1312-1316. doi:10.1016/j.bpj.2015.07.052

James ZM, Zagotta WN (2017) Structural insights into the mechanisms of CNBD channel function. *J Gen Physiol*. doi:10.1085/jgp.201711898

Jenke M, Sanchez A, Monje F, Stuhmer W, Weseloh RM, Pardo LA (2003) C-terminal domains implicated in the functional surface expression of potassium channels. *EMBO J* 22:395-403. doi:10.1093/emboj/cdg035

Ju, M., and Wray, D. (2006). Molecular regions responsible for differences in activation between heag channels. *Biochem Biophys Res Commun* 342:1088-1097. 10.1016/j.bbrc.2006.02.062.

Kotler O, Gutnick MJ, Fleidervish IA (2022) In computational models, action potential propagation in ultrathin axons is resilient despite considerable intracellular Na(+) accumulation. *Proc Natl Acad Sci USA* 119:e2120782119. doi:10.1073/pnas.2120782119

Lörinczi É, Gómez-Posada JC, de la Peña P, Tomczak AP, Fernández-Trillo J, Leipscher U, Stühmer W, Barros F, Pardo LA (2015) Voltage-dependent gating of KCNH potassium channels lacking a covalent link between voltage-sensing and pore domains. *Nat Commun* 6:6672. doi:10.1038/ncomms7672

Lörinczi E, Helliwell M, Finch A, Stansfeld PJ, Davies NW, Mahaut-Smith M, Muskett FW, Mitcheson JS (2016) Calmodulin Regulates Human Ether à Go-Go 1 (hEAG1) Potassium Channels through Interactions of the Eag Domain with the Cyclic Nucleotide Binding Homology Domain. *J Biol Chem* 291:17907-17918. doi:10.1074/jbc.M116.733576

Ludwig, J., Terlau, H., Wunder, F., Bruggemann, A., Pardo, L.A., Marquardt, A., Stuhmer, W., and Pongs, O. (1994). Functional expression of a rat homologue of the voltage gated either a go-go potassium

channel reveals differences in selectivity and activation kinetics between the Drosophila channel and its mammalian counterpart. *EMBO J* 13: 4451-4458. 10.1002/j.1460-2075.1994.tb06767.x.

Malak OA, Gluhov GS, Grizel AV, Kudryashova KS, Sokolova OS, Loussouarn G (2019) Voltage-dependent activation in EAG channels follows a ligand-receptor rather than a mechanical-lever mechanism. *J Biol Chem*. doi:10.1074/jbc.RA119.007626

Mandala VS, MacKinnon R (2022) Voltage-sensor movements in the Eag Kv channel under an applied electric field. *Proc Natl Acad Sci USA* 119:e2214151119. doi:10.1073/pnas.2214151119

Morais Cabral JH, Lee A, Cohen SL, Chait BT, Li M, Mackinnon R (1998) Crystal structure and functional analysis of the HERG potassium channel N terminus: a eukaryotic PAS domain. *Cell* 95:649-655. doi:10.1016/s0092-8674(00)81635-9

Nunez E, Muguruza-Montero A, Villarroel A (2020) Atomistic Insights of Calmodulin Gating of Complete Ion Channels. *Int J Mol Sci* 21. doi:10.3390/ijms21041285

O'Connell D, Mruk K, Rocheleau JM, Kobertz WR (2011) Xenopus laevis oocytes infected with multi-drug-resistant bacteria: implications for electrical recordings. *J Gen Physiol* 138:271-277. doi:10.1085/jgp.201110661

Parker I, Choi J, Yao Y (1996) Elementary events of InsP3-induced Ca2+ liberation in Xenopus oocytes: hot spots, puffs and blips. *Cell Calcium* 20:105-121. doi:10.1016/s0143-4160(96)90100-1

Patlak JB (1999) Cooperating to unlock the voltage-dependent K channel. *J Gen Physiol* 113:385-388. doi:10.1085/jgp.113.3.385

Rhyner JA, Koller M, Durussel-Gerber I, Cox JA, Strehler EE (1992) Characterization of the human calmodulin-like protein expressed in Escherichia coli. *Biochemistry* 31:12826-12832. doi:10.1021/bi00166a017

Sahoo N, Schonherr R, Hoshi T, Heinemann SH (2012) Cysteines control the N- and C-linker-dependent gating of KCNH1 potassium channels. *Biochim Biophys Acta* 1818:1187-1195. doi:10.1016/j.bbamem.2012.01.021

Schonherr R, Hehl S, Terlau H, Baumann A, Heinemann SH (1999) Individual subunits contribute independently to slow gating of bovine EAG potassium channels. *J Biol Chem* 274:5362-5369. doi:10.1074/jbc.274.9.5362

Schonherr R, Lober K, Heinemann SH (2000) Inhibition of human ether a go-go potassium channels by Ca(2+)/calmodulin. *EMBO J* 19:3263-3271. doi:10.1093/emboj/19.13.3263

Schonherr R, Lober K, Heinemann SH (2000) Inhibition of human ether a go-go potassium channels by Ca(2+)/calmodulin. *The EMBO journal* 19:3263-3271

Silverman WR, Bannister JPA, Papazian DM (2004) Binding Site in Eag Voltage Sensor Accommodates a Variety of Ions and is Accessible in Closed Channel. *Biophysical Journal* 87:3110-3121. doi:10.1529/biophysj.104.044602

Silverman WR, Tang CY, Mock AF, Huh KB, Papazian DM (2000) Mg(2+) modulates voltage-dependent activation in ether-a-go-go potassium channels by binding between transmembrane segments S2 and S3. *Journal of General Physiology* 116:663-678. doi:10.1085/jgp.116.5.663

Stevens-Sostre WA, Flores-Aldama L, Bustos D, Li J, Morais-Cabral JH, Delemotte L, Robertson GA (2024) An intracellular hydrophobic nexus critical for hERG1 channel slow deactivation. *Biophys J*. doi:10.1016/j.bpj.2024.01.010

Stuhmer W (1992) Electrophysiological recording from Xenopus oocytes. *Methods Enzymol* 207:319-339. doi:10.1016/0076-6879(92)07021-f

Tang C-Y, Bezanilla F, Papazian DM (2000) Extracellular Mg2+ Modulates Slow Gating Transitions and the Opening of Drosophila Ether-à-Go-Go Potassium Channels. *J Gen Physiol* 115:319-338. doi:10.1085/jgp.115.3.319

Terlau H, Heinemann SH, Stuhmer W, Pongs O, Ludwig J (1997) Amino terminal-dependent gating of the potassium channel rat eag is compensated by a mutation in the S4 segment. *J Physiol* 502:537-543. doi:10.1111/j.1469-7793.1997.537bj.x

Terlau H, Ludwig J, Steffan R, Pongs O, Stühmer W, Heinemann S (1996) Extracellular Mg2+ regulates activation of rat eag potassium channel. *Pflügers Arch Eur J Physiol* 432:301-312. doi:10.1007/s004240050137

Tian MQ, Li RK, Yang F, Shu XM, Li J, Chen J, Peng LY, Yu XH, Yang CJ (2023) Phenotypic expansion of KCNH1-associated disorders to include isolated epilepsy and its associations with genotypes and molecular sub-regional locations. *CNS Neurosci Ther* 29:270-281. doi:10.1111/cns.14001

Tomczak AP, Fernández-Trillo J, Bharill S, Papp F, Panyi G, Stühmer W, Isacoff EY, Pardo LA (2017) A new mechanism of voltage-dependent gating exposed by K_V10.1 channels interrupted between voltage sensor and pore. *J Gen Physiol* 149:577-593. doi:10.1085/jgp.201611742

Toplak Z, Hendrickx LA, Abdelaziz R, Shi X, Peigneur S, Tomasic T, Tytgat J, Peterlin-Masic L, Pardo LA (2022) Overcoming challenges of HERG potassium channel liability through rational design: Eag1 inhibitors for cancer treatment. *Med Res Rev* 42:183-226. doi:10.1002/med.21808

Tsien R, Pozzan T (1989) [14] Measurement of cytosolic free Ca2+ with quin2. *Methods Enzymol* 172: 230-262. doi:10.1016/S0076-6879(89)72017-6

Verkest C, Schaefer I, Nees TA, Wang N, Jegelka JM, Taberner FJ, Lechner SG (2022) Intrinsically disordered intracellular domains control key features of the mechanically-gated ion channel PIEZO2. *Nat Commun* 13:1365. doi:10.1038/s41467-022-28974-6

Wang W, MacKinnon R (2017) Cryo-EM Structure of the Open Human Ether-à-go-go -Related K + Channel hERG. *Cell* 169:422-430.e410. doi:10.1016/j.cell.2017.03.048

Wang Z-J, Soohoo SM, Tiwari PB, Piszczek G, Brelidze TI (2020) Chlorpromazine binding to the PAS domains uncovers the effect of ligand modulation on EAG channel activity. *J Biol Chem*:jbc.RA119.012377. doi:10.1074/jbc.RA119.012377

Wang ZJ, Ghorbani M, Chen X, Tiwari PB, Klauda JB, Brelidze TI (2023) Molecular mechanism of EAG1 channel inhibition by imipramine binding to the PAS domain. *J Biol Chem* 299:105391. doi:10.1016/j.jbc.2023.105391

Whicher JR, MacKinnon R (2016) Structure of the voltage-gated K+ channel Eag1 reveals an alternative voltage sensing mechanism. *Science* 353:664-669. doi:10.1126/science.aaf8070

Whicher JR, MacKinnon R (2019) Regulation of Eag1 gating by its intracellular domains. *eLife* 8. doi:10.7554/eLife.49188

Wynia-Smith SL, Gillian-Daniel AL, Satyshur KA, Robertson GA (2008) hERG gating microdomains defined by S6 mutagenesis and molecular modeling. *J Gen Physiol* 132:507-520. doi:10.1085/jgp.200810083

Yang Y, Ramamurthy B, Neef A, Xu-Friedman MA (2016) Low Somatic Sodium Conductance Enhances Action Potential Precision in Time-Coding Auditory Neurons. *J Neurosci* 36:11999-12009. doi:10.1523/JNEUROSCI.1475-16.2016

Zhang M, Shan Y, Pei D (2023) Mechanism underlying delayed rectifying in human voltage-mediated activation Eag2 channel. *Nat Commun* 14:1470. doi:10.1038/s41467-023-37204-6

Zhao Y, Goldschen-Ohm MP, Morais-Cabral JH, Chanda B, Robertson GA (2017) The intrinsically liganded cyclic nucleotide–binding homology domain promotes KCNH channel activation. *The Journal of General Physiology*. doi:10.1085/jgp.201611701

Ziechner U, Schönherr R, Born A-K, Gavrilova-Ruch O, Glaser RW, Malesevic M, Küllertz G, Heinemann SH (2006) Inhibition of human ether à go-go potassium channels by Ca2+/calmodulin binding to the cytosolic N- and C-termini. *FEBS J* 273:1074-1086. doi:10.1111/j.1742-4658.2006.05134.x